

Type II-Plateau supernova radiation: dependencies on progenitor and explosion properties

Luc Dessart,^{1*} D. John Hillier,² Roni Waldman,³ and Eli Livne.³

¹: Aix Marseille Université, CNRS, LAM (Laboratoire d'Astrophysique de Marseille), UMR 7326, 13388, Marseille, France

² Department of Physics and Astronomy & Pittsburgh Particle Physics, Astrophysics, and Cosmology Center (PITT PACC), University of Pittsburgh, Pittsburgh, PA 15260, USA

³: Racah Institute of Physics, The Hebrew University, Jerusalem 91904, Israel

Accepted 2013 May 13. Received 2013 May 13; in original form 2013 March 13

ABSTRACT

We explore the properties of Type II-Plateau (II-P) supernovae (SNe) together with their red-supergiant (RSG) star progenitors. Using MESA STAR, we modulate the parameters (e.g., mixing length, overshoot, rotation, metallicity) that control the evolution of a $15 M_{\odot}$ main-sequence star to produce a variety of physical pre-SN models and SN II-P ejecta. We extend previous modeling of SN II-P radiation to include photospheric and nebular phases, as well as multi-band light curves and spectra. Our treatment does not assume local thermodynamic equilibrium, is time dependent, treats explicitly the effects of line blanketing, and incorporates non-thermal processes. We find that the color properties of SNe II-P require large model atoms for Fe I and Fe II, much larger than adopted in Dessart & Hillier (2011). The color properties also imply RSG progenitors of limited extent ($\sim 500 R_{\odot}$) — larger progenitor stars produce a SN II-P radiation that remains too blue for too long. This finding calls for a reduction of RSG radii, perhaps through a strengthening of convective energy transport in RSG envelopes. Increased overshoot and rotation reduce the ratio of ejecta to helium-core mass, similarly to an increase in main-sequence mass, and thus complicate the inference of progenitor masses. In contrast to the great sensitivity on progenitor radius, SN II-P color evolution appears insensitive to variations in explosion energy. Finally, we document the numerous SN II-P signatures that vary with progenitor metallicity, revealing their potential for metallicity determinations in the nearby and distant Universe.

Key words: radiation hydrodynamics – radiative transfer – stars: atmospheres – stars: evolution – supernovae: general – stars: supernovae: individual: 1999em.

1 INTRODUCTION

Since the 1970s, red-supergiant (RSG) stars have been recognized as the potential progenitors of Type II-Plateau (II-P) supernovae (SNe; Grassberg et al. 1971; Falk & Arnett 1977). The association of RSG with Type II-P SNe has been confirmed by the detection of the progenitor star in pre-explosion images (e.g., Smartt 2009). In current surveys, they represent about 50% of all core-collapse SNe (Arcavi et al. 2010; Smith et al. 2011). The early radiation-hydrodynamics simulations of SN II-P light curves have been upgraded in recent years with improved transport (in particular with the code STELLA of Blinnikov et al. 1998) and with dedicated studies of well-observed SNe II-P, although generally limited to grey radiation transport (Utrobin 2007; Dessart et al. 2010b,a; Bersten et al. 2011; Pumo & Zampieri 2011). An alternate approach is to model the dynamical phase of the SN with grey trans-

port and switch to more sophisticated radiative-transfer schemes when the ejecta is in homologous expansion. Kasen & Woosley (2009) followed this approach by combining KEPLER hydrodynamical inputs of RSG explosions (Weaver et al. 1978) with SEDONA for the subsequent radiative transfer modeling to study SN II-P light curves. However, little information was extracted from the spectra to assess the properties of the progenitor star. This aspect is difficult to address because it requires a treatment of the gas in full non-local thermodynamic equilibrium (non-LTE; Dessart & Hillier 2011), a treatment of time-dependent ionization (Utrobin & Chugai 2005; Dessart & Hillier 2008a), and a treatment of line blanketing due to metal species (Hoeftlich 1988; Eastman et al. 1994; Dessart & Hillier 2010; Li et al. 2012). Focusing primarily on the early-time light curves, these studies do not exploit the information from nebular epochs, apart from the inference of the original mass of ^{56}Ni . It is only recently that dedicated studies of the nebular phase of SNe II-P have sought information on the progenitor helium core (Dessart & Hillier 2011; Dessart et al. 2010a;

* email: Luc.Dessart@oamp.fr

Maguire et al. 2012; Jerkstrand et al. 2012). Inferring the *ejecta* mass requires not just the inference of the H-rich envelope mass through the modeling of the photospheric-phase light curve and spectra, but also of the helium-core mass, from nebular-phase studies.

In Dessart & Hillier (2011), we presented exploratory simulations of SN II-P radiation from 10 d until 3 yr after explosion, thus covering from photospheric to nebular conditions. Over this time span, the spectrum formation region scans the entire ejecta, from the surface of the progenitor at early times down to the inner ejecta at late times. While the non-LTE time-dependent treatment of radiation transport produced a promising match to the fundamental SN II-P properties, our models overestimated the bolometric luminosity and were too blue. Two progenitor masses were used (15 and 25 M_{\odot} on the main sequence), but no parameter variation was allowed for in either the pre-SN evolution or the explosion.

There is much debate today about the progenitor masses of SNe II-P (Smartt 2009; Utrobin & Chugai 2009; Dessart et al. 2010a; Jerkstrand et al. 2012) but this is just one of numerous issues about SN II-P progenitors that need study. Being end-points of stellar evolution, their properties are controlled by nuclear reactions, opacities, energy transport, fluid instabilities in stellar interiors, as well as variations associated with initial rotation or metallicity (Woosley et al. 2002). The treatment of convection by means of the mixing-length theory (MLT), or core overshooting at the edge of convective regions, is far from satisfactory (Meakin & Arnett 2007).

One of our goals is to use SN II-P radiation to help constrain the processes that control stellar evolution, i.e., the associated parameters that appear in the stellar structure and evolution equations. We want to determine the influence of these parameters on the final properties of massive stars at death and how these connect to SN II-P radiation properties. In this study, we undertake a limited investigation of the influence of the MLT parameter, rotation, mass loss, core-overshooting, and metallicity for a 15 M_{\odot} progenitor star. To complement this, we also investigate the effect of varying the SN II-P explosion energy. This is in the spirit of Utrobin (2007), but now the diversity of progenitor/ejecta is produced by modeling the diverse evolutionary paths followed by a massive star from the main sequence until death. In other words, rather than crafting a pre-SN star in hydrostatic equilibrium, we adopt different parameters controlling stellar evolution and compute physical models of a massive star as it evolves from the main sequence until core collapse. With this approach, we can connect the radiation properties of SN II-P model ejecta to the pre-SN star and infer the parameters that influenced its evolution.

In SNe II-P, the light curve is primarily determined by the influence of the shock on the progenitor envelope and the resulting temperature and density structure of the ejecta. Thus having a physical progenitor model is crucial for understanding and predicting the light curve. The non-LTE effects, and the radiative transfer are crucial for spectral formation, and for obtaining accurate colors.

In this paper, we start off by reviewing the successes and failures of Dessart & Hillier (2011). We present the physical improvements that are necessary to obtain a better agreement with observations (Section 2). We explore in particular the color problem of our previous SN II-P simulations with CMFGEN when confronted to observations of SN 1999em. To find the origin of this problem, we use MESA STAR (Paxton et al. 2011, 2013) to generate a grid of 15 M_{\odot} models evolved from the main sequence until iron-core collapse. This grid is selected to cover parameters known to impact the evolution of massive stars and in particular their properties

at core collapse. In Section 3, we present the properties of these simulations at the onset of collapse. We also discuss the properties of the ejecta produced through a piston-driven explosion with $\dot{\text{I}}\text{d}$ (Livne 1993; Dessart et al. 2010b,a), with allowance for explosive nucleosynthesis. In Section 4, we describe the CMFGEN light curve and spectra for the whole grid of models evolved until core collapse with MESA STAR, and subsequently exploded with $\dot{\text{I}}\text{d}$. In Section 5, we first present a comparison of SN II-P radiation properties computed with CMFGEN (Hillier & Miller 1998; Dessart & Hillier 2005, 2008b; Hillier & Dessart 2012) for two 15 M_{\odot} stars that share similar properties at death but were evolved with KEPLER (model s15e12 of Dessart & Hillier 2011) and MESA STAR. We then discuss the dependencies of this radiation on progenitor and explosion properties, and specifically the impact of progenitor radius (Section 6), core overshooting (Section 7), metallicity (Section 8), and explosion energy (Section 9). We conclude and discuss the implications of our results in Section 10. Throughout this work, we compare our results to a well-observed SN II-P representative of the II-P class of objects. We choose SN 1999em (Hamuy et al. 2001; Leonard et al. 2002), and adopt the distance of 11.5 Mpc and reddening $E(B - V) = 0.1$ mag inferred by Dessart & Hillier (2006). We delay a thorough comparison to the broad class of SNe II-P to a subsequent study.

2 COMPARISON WITH Dessart & Hillier (2011)

2.1 Successes/failures of SN II-P models presented in Dessart & Hillier (2011)

Dessart & Hillier (2011) presented SN II-P time-dependent non-LTE radiative transfer simulations, covering the photospheric phase, the transition to the nebular phase, and the nebular phase until three years after the explosion of a RSG star. The progenitor evolution was computed until core collapse with KEPLER for two stars, 15 and 25 M_{\odot} on the main sequence, without rotation and at solar metallicity. With such inputs, Dessart & Hillier (2011) reproduced the basic morphology of SN II-P light curves, the length and brightness of the plateau, the typical spectral evolution from optically-thick to optically-thin conditions. Balmer lines appear strong throughout the recombination phase, a feature associated with a time-dependent effect on the ionization (Utrobin & Chugai 2005; Dessart & Hillier 2008b). This effect influences all lines to some extent. The ejecta kinetic energy of 1.2 B, the ejecta mass of $\sim 11 M_{\odot}$ and the ^{56}Ni mass of $\sim 0.08 M_{\odot}$ in model s15e12 (now referred to as model s15O for s15 “old”; see Table 1 for ejecta and progenitor parameters) appear roughly compatible with the SN 1999em characteristics at all times, including the pseudo-continuum due to Fe II and the fine structure lines associated with O I and Ca II at about one year after explosion.

At the quantitative level, a number of discrepancies are apparent. First, the representative plateau luminosity (taken at 50 d after explosion) is $\sim 6 \times 10^8 L_{\odot}$ for the s15O (formerly named s15e12) model and $10^9 L_{\odot}$ for the s25e12 model, both greater by a factor of 2-3 than inferred from standard SNe II-P (Bersten & Hamuy 2009). SN II-P simulations of Kasen & Woosley (2009), which are based on very similar KEPLER ejecta inputs have comparable plateau luminosities (within 10% of our values), and thus share the same discrepancy. Second, our s15O model exhibits a bell-shape V -band light curve (the R and I band light curves have a similar morphology), instead of the plateau generally observed. Probably related, our predicted U -band light curve fades too slowly, even exhibiting a rise or a plateau at early times in model s25e12. This was

observed by Gezari et al. (2008), but for about a week only. Even in those events detected soon after explosion, SNe II-P exhibit a U -band fading after discovery (Quimby et al. 2007; Brown et al. 2007, 2009). The B -band light curve may show a short rise at first, but within a week initiates a fading. Hence, our simulations are too luminous and tend to remain blue for too long. Third, the nebular phase spectra of Dessart & Hillier (2011) systematically predict no $H\alpha$ emission although a strong line is observed (in, e.g., SN 1999em; Leonard et al. 2002). In the Dessart & Hillier (2011) SN II-P ejecta models, significant mixing is applied, making hydrogen present in the inner ejecta, so the discrepancy is unlikely caused by insufficient mixing. Finally, the transition from thick to thin conditions at the end of the plateau comes in Dessart & Hillier (2011) with a sudden disappearance of continuum-like flux — the spectrum suddenly becomes a pure emission spectrum (as in a genuine nebula) while SNe II-P exhibit a pseudo-continuum for months after the end of the plateau. This transition phase between thick and thin conditions is not modelled in detail by any other code in the community so we cannot compare our synthetic spectra with alternate works.

2.2 Improvements since Dessart & Hillier (2011)

Before invoking inadequate progenitor or explosion properties, we must first investigate shortcomings potentially affecting the radiative-transfer solution. We identify three limitations to the Dessart & Hillier (2011) approach:

(i) Insufficient opacity: This is a major concern for any radiative-transfer modeling of astrophysical plasmas, in particular in association with metal line blanketing. Dessart & Hillier (2011) discussed the important role of sub-dominant species like Sc II, Ti II, or Cr II during the recombination phase. Li et al. (2012) emphasized the importance of Fe I to correct (at least in part) the overestimate in the U -band flux for SN 1987A models (Dessart & Hillier 2010). In Dessart & Hillier (2011), we employed a modest model atom for iron, with 136 levels for Fe I and 115 levels for Fe II. The models also lacked the neutral state for many species, including Ne, Mg, Si, S, Ar, K, and Ca.

(ii) Neglect of non-thermal processes: As demonstrated by Lucy (1991); Kozma & Fransson (1992, 1998a,b); Li et al. (2012); Dessart et al. (2012), γ -rays from radioactive decay give rise to high-energy electrons that can non-thermally excite and ionize the gas, exacerbating the departures from LTE. Such non-thermal processes thrive in low-ionization conditions, which prevail in SNe II-P during the recombination phase and beyond. The energy channeled into excitation and ionization reduces the fraction going into heat and reduces the gas temperature. Hence, the simulations of Dessart & Hillier (2011) do not model the non-LTE properties of the gas adequately, particularly during the nebular phase.

(iii) Assumption of local energy deposition: While the γ -ray mean free path remains small compared to the scale of the ejecta, preventing γ -ray escape, γ -rays may leak out of the core and deposit their energy within the overlying H-rich envelope. Local energy deposition underestimates the contribution of the envelope to the emergent spectrum (Maguire et al. 2012).

In a new simulation, named s15N (for s15 “new”), we re-run the model s15 with a large model atom for Fe I (1142 levels; 77420 transitions) and Fe II (827 levels; 44831 transitions). We include additional neutral species, and specifically Ne I, Mg I, Si I, S I, Ar I, Ar II, K I, Ca I. We treat non-thermal processes as explained and tested in Li et al. (2012); Dessart et al. (2012). We also allow for

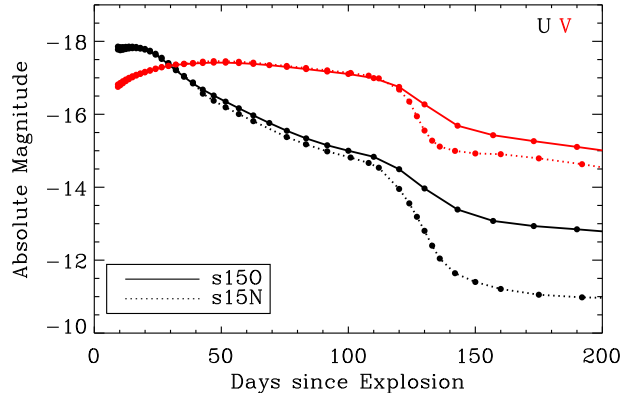


Figure 1. Comparison between the absolute U -band (black) and V -band (red) synthetic light curves for models s15O (solid; i.e., model s15 “old”) and s15N (dotted; i.e., model s15 “new”) as a function of days since explosion. The differences, most visible at nebular times, stem from the use of bigger Fe I and Fe II model atoms and the treatment of non-thermal processes and non-local energy deposition in model s15N.

non-local energy deposition by solving the γ -ray transport problem at each time step (Hillier & Dessart 2012). However, we keep the same hydrodynamical input (i.e., s15e12) for s15N as previously used for s15O.

During a model sequence, we adjust the size of the model atoms to have the most complete description of opacity sources. At early times, the wide range in ionization forces us to include Fe I to Fe VII while late in the plateau phase, only Fe I to Fe IV are needed. When we reduce the number of ions to treat, we increase the number of levels for the dominant ions. As a result, the total number of levels and transitions varies along any given sequence. For model s15N, we treat a total of 8308 levels and 197499 bound-bound transitions up to day 60, 7103 levels and 220993 transitions from day 60 to day 130, and 5281 levels and 188457 transitions beyond 130 d.

In our approach, we typically include all the metal line transitions with a gf value greater than 0.002 at early times. When metal line blanketing becomes visible in the spectrum, we lower this value to 0.0001. However, this cut only applies to elements whose atomic weight is greater than 20, does not apply to the lowest n levels (n is typically 9), and a transition is omitted only when there is at least m (m is typically 9) stronger downward transitions from the level. Thus, this procedure does not cut important transitions to ground levels, and forbidden and semi-forbidden transitions among low-lying states. With this procedure, we include lines in a very different way from that used in some SN Ia studies (Kasen et al. 2008), which use a gf cut alone for the selection. We have performed numerous tests and we find that the large model atoms we employ in this work for metal species yield converged results (see also Dessart & Hillier 2011; Li et al. 2012), i.e., increasing further the size of model atoms does not influence noticeably the emergent spectra and colors. The much larger number of lines quoted in SNe Ia studies also stems from their stronger impact in H-deficient ejecta, where, unlike in SNe II, metal line blanketing is the primary source of opacity.

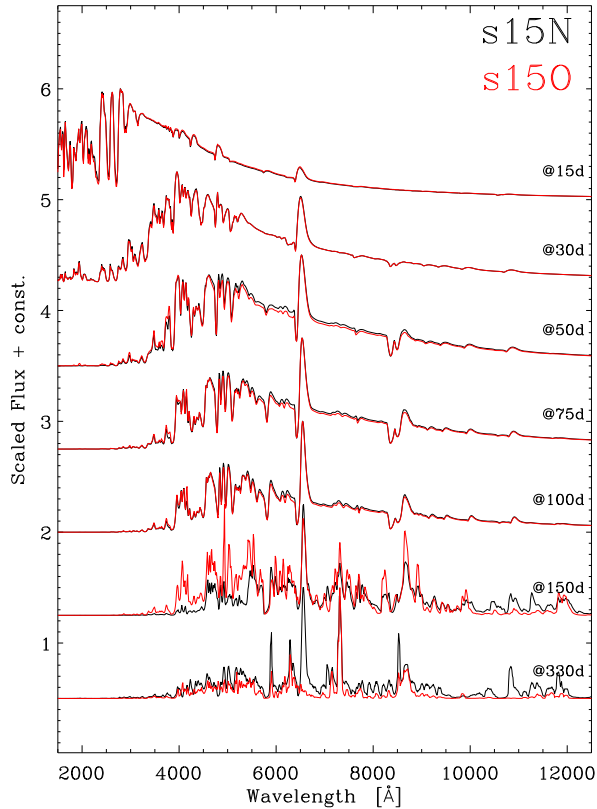


Figure 2. Comparison of the spectral evolution at photospheric and nebular times for models s15N (black) and s15O (red). Notice the modest differences during the photospheric phase, the stronger blanketing in the s15N model at early nebular times, and the prediction of strong H α throughout the nebular phase in model s15N. We present line identifications at multiple epochs in Figs. A1–A4.

2.3 New results

During the photospheric phase, we obtain little difference in color (Fig. 1) and spectral properties (Fig. 2) between models s15N and s15O. However, when the ejecta becomes nebular, line blanketing from both Fe I and Fe II weaken the flux shortward of 6000 Å and increase it in the red, primarily in the form of line emission. The impact on the *V* band light curve is noticeable although modest, while the effect in the *U* band is huge. At the times shown, model s15N is systematically 2 magnitudes fainter than model s15O in the *U* band. The luminosity of the SN model is the same; the enhanced blanketing redistributes the flux and changes the lines that act as coolant for the ejecta. In between strong emission lines, there is also additional flux from overlapping weak lines (associated especially with Fe I and Fe II), whose cumulative effect mimics a pseudo-continuum.

Recently, Li et al. (2012) have discussed the influence of non-thermal processes in the Type II-pec SN 1987A, and in particular their decisive role for enhancing or maintaining the Balmer line strength/width when the SN becomes nebular. Non-thermal processes have a direct impact on level excitation and species ionization. Because they increase the population of excited levels, they can also favor indirectly the photoionization rates. As in SN Ib/c where non-thermal processes are key for the production of He I lines, we find that they are essential in SNe II-P to produce strong

H α and He I 10830 Å. In model s15N, both lines are present when no equivalent feature is seen in s15O (Fig. 2). We also predict He I 7065 Å but it is overestimated compared to observations of SN 1999em (the same problem occurs in a SN II-pec model when compared to SN 1987A Li et al. (2012)). The nebular models of Jerkstrand et al. (2012) do not predict an observable He I 7065 Å. However the assumed structure of their models during the nebular phase is very different from that assumed here. The hydrogen (helium) ionization is higher by two (ten) orders of magnitude in the inner ejecta in model s15N compared to model s15O at 300 d after explosion. However, hydrogen and helium remain primarily neutral so the associated dominant ions are H I and He I in both s15N and s15O.

Prior to ~ 300 d after explosion, the decay energy is trapped within the ejecta in all our simulations. However, as early as 100–200 d, some γ -rays can escape the core and deposit their energy in the inner H-rich ejecta. This causes a temperature reduction of ~ 1000 K in ejecta shells with $v \lesssim 2000$ km s $^{-1}$ at 300 d between models s15N and s15O, aggravated by the channeling of that energy into non-thermal excitation/ionization. In contrast, the overlying H-rich shells of the s15N ejecta are typically 2000–3000 K hotter than those of model s15O where local-energy deposition is assumed.

The inclusion of additional neutral species gives rise to lines not predicted in Dessart & Hillier (2011). Because of their low ionization potentials, these are present at nebular times, i.e., beyond the end of the plateau and/or later. In this set, we have the K I resonance line at 7600 Å,¹ Mg I lines (primarily in the near-IR), while Si I, S I and Ca I lines, which are predicted in pair-instability SN nebular spectra (Dessart et al. 2013), remain too weak to be visible here. We find lines that form preferentially in what used to be the progenitor core (e.g., the doublet [Ca II] 7300 Å and He I 7065 Å), or preferentially in the H-rich ejecta shells (H α), and lines that form in both (e.g., [O I] 6300 Å doublet, He I 10830 Å, Fe II 5169 Å, and the Ca II triplet at 8500 Å). Na I D hardly changes between models s15N and s15O. This is expected since it is a resonance line; it scatters whatever overlapping background flux is emitted from deeper ejecta layers. Some illustrations of line identifications are provided in the appendix, in Figs. A1–A4.

Overall, the agreement between model s15N and SN 1999em is much better than with s15O (Fig. 3 and Fig. 4), which implies that employing a large model atom, in particular for iron, and treating non-thermal processes are both important for the modeling of SNe II-P (non-local energy deposition is less influential within the first year of a SN II-P). However, some problems remain. Our model plateau luminosity for SN 1999em is still too high, the *V/R/I*-band light curves still exhibit a peculiar bell shape, and the *U*-band flux is still too slowly decreasing with time compared to observations.

Given that all our attempts to resolve this remaining color problem have failed, the mismatch may after all be physical. In particular, it does not seem to be related to an opacity issue. The solution may be found in alternate progenitor and/or explosion models. Intuitively, it could be related to the energy budget of the ejecta, with the slower-than-observed cooling of the photosphere (fading of the UV, *U*, and *B*-band regions) associated with a RSG progen-

¹ This line, blended with O I 7777 Å, is mentioned by Chornock et al. (2010) to explain the observed 7770 Å feature in SN 2006ov. We find that in general, past the end of the plateau phase, the broad feature is primarily due to K I.

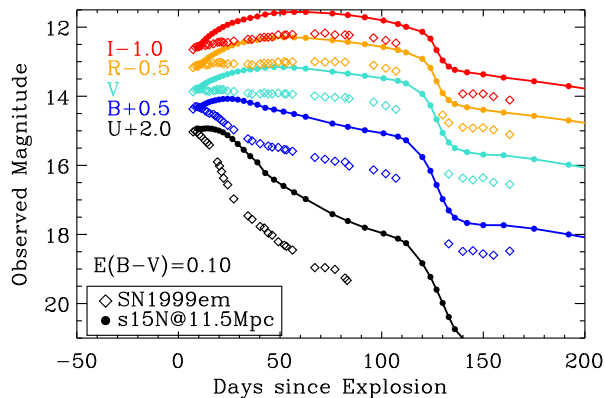


Figure 3. Comparison between the s15N model (reddened with $E(B - V) = 0.10$ mag and the extinction law of Cardelli et al. 1988) and the multi-band light curves of SN 1999em, scaled to the SN distance of 11.5 Mpc (Dessart & Hillier 2006).

itor radius, as produced by stellar evolution, that is generally too large.

3 GRID OF MESA STAR COMPUTATIONS FOR A $15 M_{\odot}$ MAIN-SEQUENCE STAR

The previous sections suggest that the CMFGEN simulation s15N based on the KEPLER model s15e12 (Dessart & Hillier 2011) reproduces most of the generic signatures of SNe II-P but fails to reproduce their color evolution. Assuming that this shift is physical and that it does not stem from inadequate explosion properties (as may be argued for the shift in plateau luminosity), we now investigate if different progenitor properties could resolve this persistent problem. To limit the parameter space, we focus on one main-sequence mass only and vary some of the parameters that control its evolution until core collapse.

Using MESA STAR, we generate a grid of models starting with the same main sequence mass of $15 M_{\odot}$. The parameters used for our reference MESA STAR simulation named m15 are solar metallicity (we take $Z = 0.02$), zero rotation, a mixing-length parameter $\alpha = 1.6$, a standard resolution (MESH_DELTA_COEFF=1), no core-overshooting, the mass loss rate recipes dubbed “Dutch” with a scaling of 0.8. Using this m15 reference model parameters, we compute a wide variety of additional models in which specific parameters are modified, covering different mixing-length parameters ($\alpha = 1.1$ and 3 for models m15mlt1 and m15mlt3), enhanced mass loss (DUTCH_WIND_ETA = 2 for model m15Mdot), an exponential overshoot parameter of 0.016 (model m15os; see Section 5.2 of Paxton et al. 2011 for a description on how overshooting is implemented), models with an equatorial velocity of 100 and 200 km s^{-1} on the zero-age main sequence (models m15r1 and m15r2), and finally models evolved at metallicities of 0.002, 0.008, 0.04 (named m15z2m3, m15z8m3, and m15z4m2). In all simulations, we adopt the Schwarzschild criterion for convection. In Table 1, we summarize the pre-SN properties for each model and show various slices through the stellar envelope at that time in Fig. 5.

At the onset of core collapse (central density of $\sim 10^9 \text{ g cm}^{-3}$), the reference model m15 (also called m15e1p3 when compared to models with different kinetic energies, or m15z2m2 when compared to models of different metallicity), is a $14.09 M_{\odot}$ RSG star

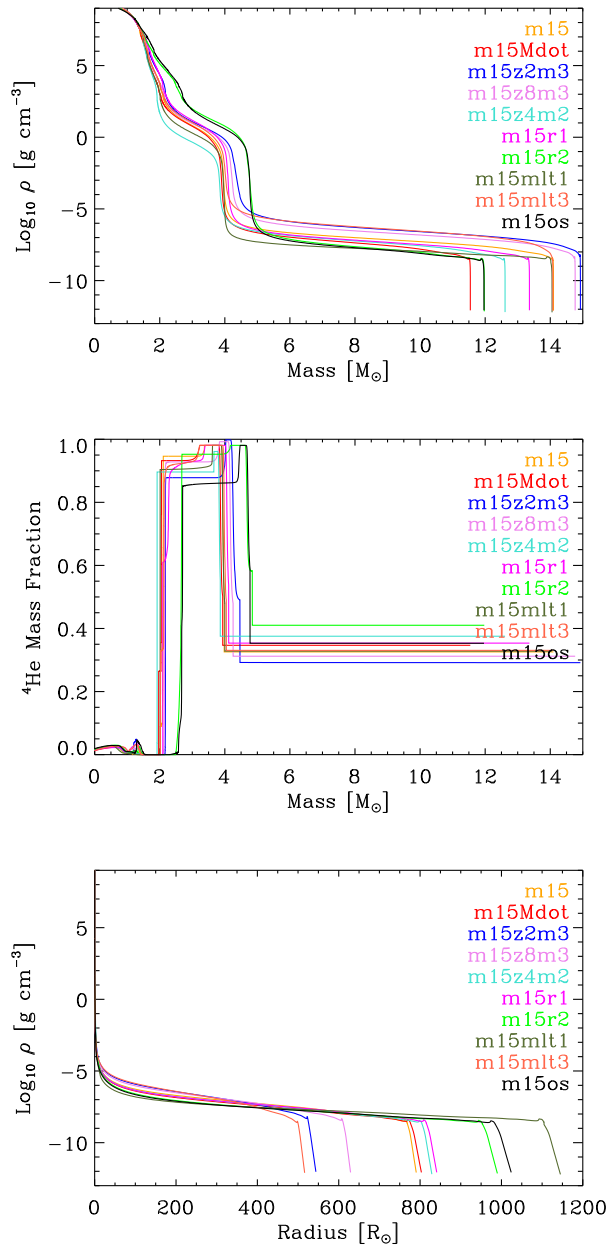


Figure 5. Slices through the MESA STAR progenitors at the onset of core collapse showing the mass density (top row) and the ${}^4\text{He}$ mass fraction (middle row) versus Lagrangian mass, and the density versus radius (bottom row). For the model nomenclature, see Section 3.

with a luminosity of $63141 L_{\odot}$, a radius of $768 R_{\odot}$, an effective temperature of 3303 K . It possesses an H-rich envelope of $10.21 M_{\odot}$, an helium core of $3.88 M_{\odot}$ (set by the inner edge of the H-rich envelope), while the outer edge of the iron core is at $1.6 M_{\odot}$ (taken here at the location when the electron fraction drops below 0.49 — at this point the ${}^{54}\text{Fe}$ mass fraction rises suddenly from 7×10^{-5} in the envelope to 0.05).

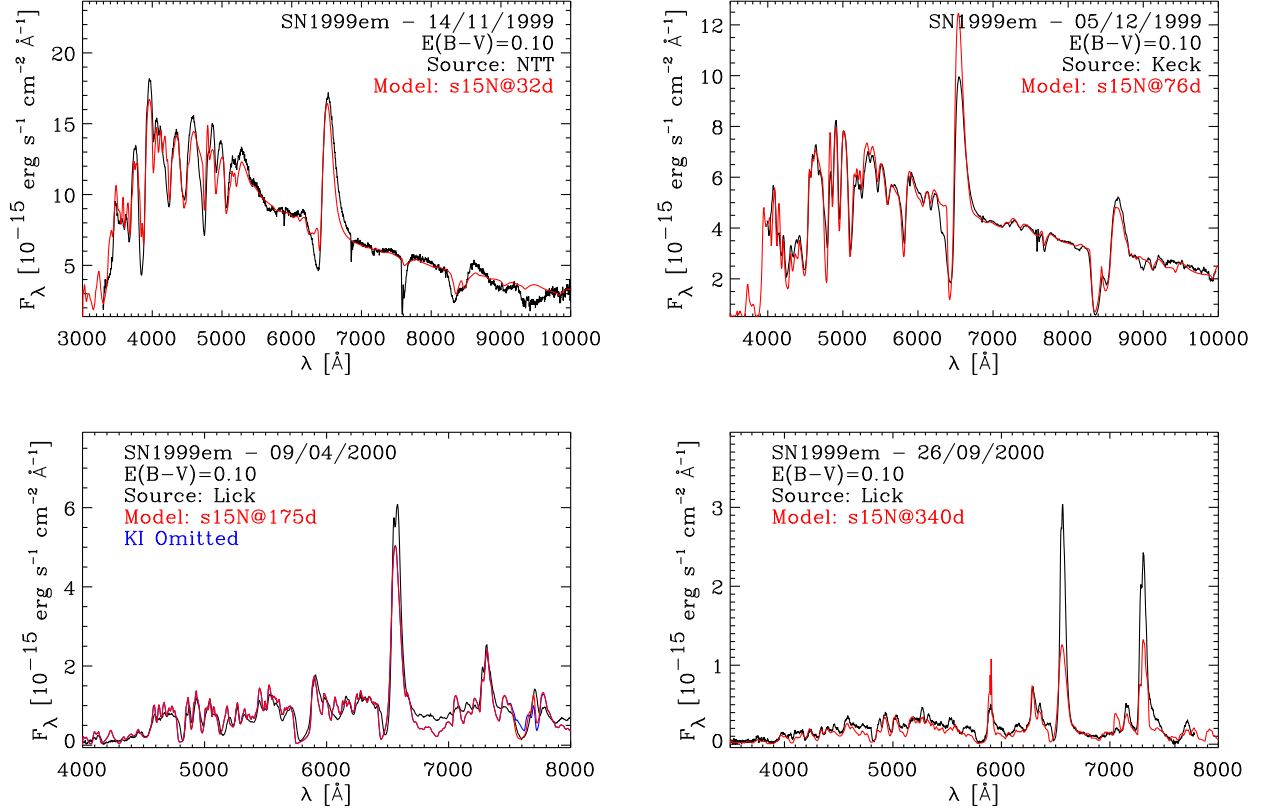


Figure 4. Spectral comparison between model s15N (reddened with $E(B - V) = 0.10$ mag and the Cardelli extinction law; Cardelli et al. 1988) and multi-epoch observations of SN 1999em, scaled to the SN distance of 11.5 Mpc (Dessart & Hillier 2006). For each epoch, a slight time shift is allowed for to correct for the mismatch in color shown in Fig. 3. In the bottom left panel, the blue curve corresponds to the synthetic flux when K I bound-bound transitions are taken out — this alters only one feature near 7600 Å associated with the resonance transition of K I.

Influence of the mixing-length parameter

In the reference model, and in fact in all RSG star models, the entire H envelope is convective. Varying the mixing-length parameter thus does not alter the fraction of the H-rich envelope that is convectively unstable, but merely modifies the efficiency of convective energy transport. We tested what stellar radius our RSG would have if energy transport in the envelope was done by radiative diffusion alone, which can be determined by reducing α to something very small (we tested with $\alpha = 0.1$). In this case, the radius increases enormously when the star becomes a RSG, becoming as large as $\sim 2500 R_{\odot}$ at the onset of collapse in our MESA STAR calculation. More realistically, we choose $\alpha = 1.1, 1.6,$ and 3 which produces RSG surface radii of $1107 R_{\odot}, 768 R_{\odot},$ and $501 R_{\odot}$ (models m15mlt1, m15mlt2, and m15mlt3). Importantly, such non-rotating solar-metallicity $15 M_{\odot}$ stars reach the RSG phase when hydrogen core/shell burning is completed. Hence, the strong convection that affects their envelopes late in their life has only a small influence on the helium core properties — uncertainties in RSG mass loss rates, because they impact the star late in its life, have little impact on the He core as well. Consequently, models m15mlt1, m15mlt2, and m15mlt3 differ primarily in surface radius (or H-rich envelope density). We use these models to gauge the impact of the RSG radius on SN II-P radiation (Section 6).

Influence of rotation

Compared to the non-rotating reference model m15, rotation produces higher mass helium cores, higher luminosities that foster a stronger mass loss rate, and more extended RSG stars at death. Enhanced initial rotation rate also leads to a smaller $M_{\text{total}}/M_{\text{He core}}$ at core collapse. Here, we employ modest initial rotational velocities of 100 and 200 km s^{-1} at the equator and on the main sequence (model m15r1 and m15r2).

Influence of core overshooting

Introducing core overshooting has a similar impact as increasing rotation (model m15os). In recent simulations of massive stars for the analysis of VLT-FLAMES survey observations, Brott et al. (2011) motivate the use of a (step-function) overshoot of 0.335 . This extends the convective zone by 0.335 times the local pressure scale height with a constant diffusion coefficient set to the value at the edge of the original convective zone. In model m15os, we employ an exponential overshoot of 0.016 , implying an exponential decrease of the diffusion coefficient according to Eq. 2 of Paxton et al. (2011). In practice, the effect of a 0.1 step-function overshoot is equivalent to an 0.008 exponential overshoot.

Using the step-function overshoot in MESA STAR, we explore the impact of this process on the evolution of a $15 M_{\odot}$ star and its properties at core collapse. We find that increasing the overshoot

parameter from 0 to 0.5 leads to a reduction of the final star mass from 13.57 to 9.40 M_{\odot} and an increase in helium core mass from 3.96 to 6.61 M_{\odot} . The ratio $M_{\text{total}}/M_{\text{He core}}$ varies from 3.42 down to 1.42, in the same order. These modulations are non trivial. The variations in pre-SN structure that result from enhanced core overshooting (or rotation) parallel those obtained for enhanced main-sequence mass, which are known to influence SN ejecta kinematics and SN II-P radiation properties (Dessart et al. 2010a).

Influence of metallicity

Because of the adopted metallicity dependence of RSG mass loss rates, our MESA STAR models m15z2m3, m15z8m3, m15 (also called model m15z2m2 in this context), and m15z4m2 have final H-rich envelope masses of 10.77–8.83 M_{\odot} . The efficiency of convective energy transport being set in all four simulations through a mixing-length parameter of 1.6, the variation in metallicity, which changes the opacity in the envelope, alters the stellar radius (since the energy flux to transport from the edge of the core to the stellar surface is essentially the same between these 4 models). Consequently, for smaller metallicities (opacities), we obtain smaller RSG radii. Our RSG models are thus both more massive and more compact at lower metallicities.

Piston-driven explosions with $\check{\text{I}}\text{d}$

Each MESA STAR model in our grid, once it has reached the onset of core collapse, is exploded with $\check{\text{I}}\text{d}$ (Livne 1993; Dessart et al. 2010b,a) by driving a piston at the inner boundary in order to yield an ejecta kinetic energy of $\sim 1.2\text{ B}$. For simplicity and to avoid biases between models, we choose the edge of the iron core to position the piston in all cases (corresponding to the $M_{r,\text{Ye}}$ in Table 1). Depending on the core properties, the combustion generates various amounts of ^{56}Ni . We make no attempt at adjusting the piston properties to yield the same ^{56}Ni mass, but we note that the explosive nucleosynthesis and fallback are quite sensitive to the exact location of the piston and its adopted trajectory. To gauge the influence of the explosion energy on the SN II-P characteristics, we also run two additional models designed to have ejecta kinetic energies of 0.6 and 2.9 B (models m15e0p6 and m15e2p9) — when these models are discussed, the reference model, which is characterized by a 1.27 B ejecta kinetic energy, is named m15e1p3.

All ejecta are mixed using a boxcar algorithm with a width of 0.4 M_{\odot} . This mixes the He-core material efficiently but leads to modest mixing of ^{56}Ni into the H-rich envelope. In practice, the sequence of m15 simulations with $\sim 1.2\text{ B}$ ejecta kinetic energies have little ^{56}Ni beyond $\sim 2000\text{ km s}^{-1}$. A final property of our ejecta models is that, suffering mild fallback, their inner velocity is often very low. This poses a challenge for CMFGEN since the velocity space to cover is much larger (say from 50 to 20000 km s^{-1}). Inevitably, this causes some numerical diffusion, whereby strong gradients are softened as we remap the grid at each time step. Furthermore, the slow inner ejecta shells expand less and remain dense out to late times, inhibiting forbidden-line emission. Our artificial piston-driven explosions are thus limited in physical consistency, potentially affecting SN observables when radiation arises from the inner ejecta, as it does at nebular times (this issue is relevant for all piston-driven explosions). Because of these limitations, we postpone a detailed investigation of the influence of mixing in our SN II-P simulations.

An important property of all RSG stars is the strong compactness of the helium core (which typically fits within 1 R_{\odot}) and the

very extended H-rich envelope. This holds for all models shown in Fig. 5, but also for RSG models of different main-sequence masses (Woosley & Heger 2007; Dessart et al. 2010b). The H-rich envelope always has a small binding energy while the helium core is highly bound. Owing much to this property, the plateau phase of SNe II-P corresponds to epochs when the photosphere is within the (originally extended) H-rich envelope and as such the plateau phase can only serve as a diagnostic of the H-rich envelope mass (Dessart & Hillier 2011). Hence, it does not (and it cannot) provide a reliable constraint on the helium core mass, nor on the ejecta mass. We stress this property because the so-called mass discrepancy emphasized by Utrobin (2007); Utrobin & Chugai (2009) seems to stem from the large inferred helium-core mass, although photospheric-phase light curve modeling constrains the H-rich envelope mass only. Furthermore, their adopted density structure seems peculiar for a RSG since only the inner 2 M_{\odot} of the progenitor model is highly bound, even for the 29 M_{\odot} main-sequence star employed for SN 2004et (Utrobin & Chugai 2009).

Summary of model nomenclature

Model s15O is based on the s15e12 ejecta model and is described in detail in Dessart & Hillier (2011). Model s15N is identical except for improvements in the radiative transfer, which are discussed in Section 2. In contrast, all models started with “m15” were computed with MESA STAR and exploded with $\check{\text{I}}\text{d}$. We divide Table 1 in groups in which a single parameter has been varied. These distinct groups include models computed with a different core-overshooting parameter (m15 and m15os), with different initial rotation rates (m15r0, m15r1, m15r2), at different metallicities (m15z2m3, m15z8m3, m15z2m2, m15z4m2), and exploded with different explosion energies (m15e0p6, m15e1p3, m15e2p9). In each sub group, the reference model m15 is used, but for clarity its name is edited to reflect the quantity that was altered. Hence, model m15 becomes m15z2m2 when compared to models computed at different metallicity etc. Similarly, we use m15r0, m15mlt2, m15e1p3.

In the following sections, we illustrate the results from simulations started from MESA STAR and $\check{\text{I}}\text{d}$ inputs, evolved with CMFGEN, and using the same setup (radiative-transfer technique, model atoms etc) as for the simulation s15N described in Sections 2.2–2.3.

4 DIVERSITY OF SN II-P RADIATION PROPERTIES FOR A 15 M_{\odot} MAIN SEQUENCE STAR

One important goal of SN II-P research is to determine the progenitor mass, both at the time of explosion and on the main sequence. In our exploration, although we use the same main-sequence mass, the different evolutionary paths associated with different metallicities, rotation rates, mixing-length parameters or mass loss rates, lead to a range of pre-SN properties (primarily final mass, He-core mass, H-rich envelope mass, radius). In turn, the resulting stellar explosions display a range of SN II-P bolometric light curves (Fig. 6), multi-band light curves (see Figs. B1–B4 for a full illustration), as well as spectral evolution.

For models characterized by the same $\sim 1.2\text{ B}$ ejecta kinetic energy, the plateau brightness varies by about a factor of 2; the plateau phase lasts between 120 and 150 d; the nebular luminosity spans a factor of ~ 7 . The plateau brightness increases with progenitor radius following the reduced cooling from expansion. The plateau length is reduced for a smaller ejecta mass

Table 1. Summary of model properties used as initial conditions for CMFGEN simulations. The quantities tabulated are in general self explanatory. Following the columns containing the cumulative ejecta masses in H, He, and O, we give the Lagrangian mass corresponding to specific locations in the pre-SN star: M_{r,Y_e} corresponds to the edge of the iron core, i.e., where the electron fraction rises to 0.49 as we progress outward from the star center (this is also the piston location for the explosion); M_{r,S_4} stands for the Lagrangian mass where the entropy above the iron core rises to $4k_B$ per baryon, $M_{r,He}$ to the base of the Helium-rich shell, and $M_{r,H}$ to the base of the H-rich envelope. The last three columns give some ejecta properties that result from the imposed explosion parameters. The quoted ^{56}Ni mass corresponds to that originally produced in the explosion. Each model was started from a $15 M_\odot$ main-sequence star, but evolved with different codes and under different conditions. For the model nomenclature, see end of Section 3.

model	M_{final} [M_\odot]	Age [Myr]	T_{eff} [K]	R_\star [R_\odot]	L_\star [L_\odot]	Z	M_{H} [M_\odot]	M_{He} [M_\odot]	M_{O} [M_\odot]	M_{r,Y_e} [M_\odot]	M_{r,S_4} [M_\odot]	$M_{r,He}$ [M_\odot]	$M_{r,H}$ [M_\odot]	$M_{\text{H,env}}$ [M_\odot]	M_{ej} [B]	E_{kin} [M_\odot]	$M_{^{56}\text{Ni}}$
s15O	12.79	13.24	3300	810	70235	0.020	5.490	4.000	0.816	...	1.72	2.93	4.13	8.66	10.93	1.20	0.087
s15N	12.79	13.24	3300	810	70235	0.020	5.490	4.000	0.816	...	1.72	2.93	4.13	8.66	10.93	1.20	0.087
m15	14.09	12.39	3303	768	63141	0.020	6.630	5.105	0.325	1.62	1.62	2.00	3.88	10.21	12.48	1.27	0.050
m15Mdot	11.53	12.65	3249	776	60426	0.020	4.839	4.444	0.316	1.50	1.61	1.95	3.81	7.72	10.01	1.28	0.081
s15N	12.79	13.24	3300	810	70235	0.020	5.490	4.000	0.816	...	1.72	2.93	4.13	8.66	10.93	1.20	0.087
m15mlt1	14.01	12.36	3318	1107	106958	0.020	6.516	5.167	0.354	1.36	1.61	2.00	3.89	10.13	12.57	1.24	0.121
m15mlt2	14.09	12.39	3303	768	63141	0.020	6.630	5.105	0.325	1.62	1.62	2.00	3.88	10.21	12.48	1.27	0.050
m15mlt3	14.08	12.41	4106	501	64218	0.020	6.542	5.173	0.383	1.54	1.55	2.02	3.92	10.16	12.52	1.34	0.086
m15	14.09	12.39	3303	768	63141	0.020	6.630	5.105	0.325	1.62	1.62	2.00	3.88	10.21	12.48	1.27	0.050
m15os	11.93	13.21	3175	984	88612	0.020	4.510	4.385	0.762	1.63	1.76	2.28	4.64	7.29	10.28	1.40	0.15
m15r0	14.09	12.39	3303	768	63141	0.020	6.630	5.105	0.325	1.62	1.62	2.00	3.88	10.21	12.48	1.27	0.050
m15r1	13.34	12.95	3277	815	68932	0.020	5.800	5.126	0.404	1.60	1.65	2.09	4.00	9.34	11.73	1.35	0.10
m15r2	11.94	14.88	3221	953	87895	0.020	4.109	5.001	0.512	1.52	1.80	2.46	4.61	7.34	10.39	1.34	0.19
m15z2m3	14.92	13.57	4144	524	72890	0.002	7.483	5.048	0.507	1.61	1.65	2.13	4.15	10.77	13.29	1.35	0.081
m15z8m3	14.76	13.34	3813	611	71052	0.008	7.183	5.252	0.428	1.63	1.65	1.90	4.09	10.67	13.12	1.27	0.036
m15z2m2	14.09	12.39	3303	768	63141	0.020	6.630	5.105	0.325	1.62	1.62	2.00	3.88	10.21	12.48	1.27	0.050
m15z4m2	12.60	10.88	3137	804	56412	0.040	5.119	5.042	0.387	1.40	1.49	1.91	3.77	8.83	11.12	1.24	0.095
m15e0p6	14.09	12.39	3303	768	63141	0.020	6.630	5.105	0.325	1.62	1.62	2.00	3.88	10.21	12.46	0.63	0.046
m15e1p3	14.09	12.39	3303	768	63141	0.020	6.630	5.105	0.325	1.62	1.62	2.00	3.88	10.21	12.48	1.27	0.050
m15e2p9	14.09	12.39	3303	768	63141	0.020	6.630	5.105	0.325	1.62	1.62	2.00	3.88	10.21	12.48	2.91	0.052

and/or a smaller progenitor radii (see also Litvinova & Nadezhin 1983; Popov 1993; Young 2004). The plateau phase starts when hydrogen-recombination sets in, which occurs when the gas temperature at the photosphere is ~ 5500 K. Subsequently, the recession of the photosphere to deeper ejecta layers occurs at a rate comparable to the expansion rate of the corresponding layers, which combined to the fixed photospheric temperature, leads to a constant luminosity. The “plateau” radii in these simulations are typically of $\sim 2 \times 10^{15}$ cm. In some models with a large ^{56}Ni mass (e.g., s15N or m15r2), the bolometric light curve shows a mild slant upward at the end of the “plateau”.

The nebular flux directly scales with the mass of ^{56}Ni synthesized in the explosion, which in our approach, increases for progenitors with a higher mass helium core. It is maximum for the m15r2 and m15os models whose helium core mass is $\sim 4.6 M_\odot$. In some models with the same helium core mass, we obtain a range of ^{56}Ni masses because of differences in inner core structures and the Lagrangian mass adopted for the piston (see Table 1). All these results are as expected, but they highlight the difficulty of inferring the progenitor mass, because it is necessarily subject to uncertainties from stellar evolution (e.g., affecting R_\star) or unknowns about the progenitor star environment (e.g., Z).

In the following sections, we study in more detail the impact on SN II-P properties arising from variations in progenitor radius (Section 6), core overshooting (Section 7), metallicity (Section 8), and explosion energy (Section 9). We first present a comparison of SN II-P radiation properties for models computed with KEPLER and MESA STAR & 1d.

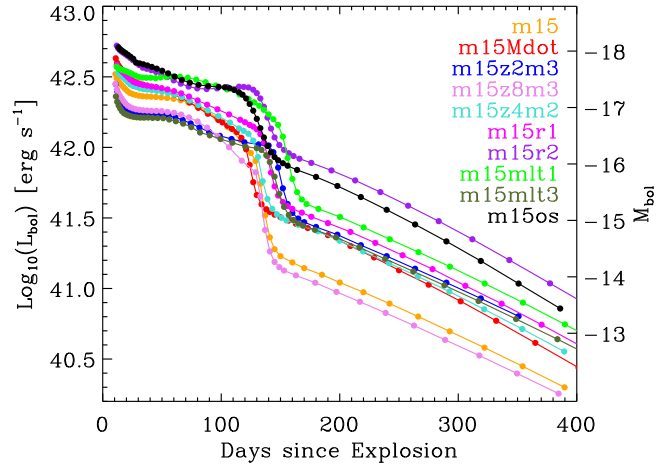


Figure 6. Bolometric light curves computed with CMFGEN and based on MESA STAR simulations for a $15 M_\odot$ main-sequence star evolved under different assumptions, and exploded the same way with 1d using a piston speed of 30000 km s^{-1} . All models in this figure are within 10% of a reference ejecta kinetic energy of 1.2 B. Models with different ejecta kinetic energies are presented in Fig. 14. [See Section 3 and Table 1 for details.]

5 COMPARISON BETWEEN KEPLER AND MESA STAR

MESA STAR is a public code and thus offers a great potential for the community to study stellar evolution and, in our field of research, produce new and diverse pre-SN massive star mod-

els, resulting from either single or binary-star evolution. A lot of benchmarking has been done in MESA STAR, some of which is described in Paxton et al. (2011, 2013). Here, we investigate what MESA STAR parameters are needed to make a $15 M_{\odot}$ main-sequence star produce a SN II-P explosion comparable to s15N, whose pre-SN evolution (and explosion) was computed with KEPLER (Woosley & Heger 2007).

Of all light curves and ejecta/envelope properties presented in Fig. 6 and Table 1, progenitor/explosion model m15Mdot is a near twin of s15N, with $R_{\star}/M_{\text{H env}}/E_{\text{kin}}/M^{56\text{Ni}}$ of $776 R_{\odot}/7.72 M_{\odot}/1.28 \text{B}/0.081 M_{\odot}$ compared to $810 R_{\odot}/8.66 M_{\odot}/1.20 \text{B}/0.087 M_{\odot}$ in s15N. The mixing imposed in model m15Mdot (which is done with the same procedure as in other m15 simulations) is weaker than in model s15N, i.e., the ^{56}Ni remains more centrally concentrated in model m15Mdot. For H and He, models m15Mdot and s15N differ in cumulative mass at the 10% level, while for subdominant species whose mass-fraction distribution tends to peak in the core, the differences are up to a factor of 2 (for example, the total oxygen mass is $0.78 M_{\odot}$ in model s15N but only $0.27 M_{\odot}$ in model m15Mdot). The progenitor core properties differ between the two simulations, in part because of the lack of core overshooting in model m15Mdot, and a much coarser nuclear network in MESA STAR that includes 21 isotopes only while model s15N contains the yields computed for over 2000 isotopes. For intermediate-mass and iron-group elements (respectively IMEs and IGEs) with known blanketing effects (e.g., Sc II, Cr II etc.; see Dessart & Hillier 2011) but not accounted for in the MESA STAR calculation, we set their abundance to the solar-metallicity value (Grevesse & Sauval 1998). Hence, in practice, the m15Mdot model has a similar H-rich envelope composition to s15N but neglects any depth variation in IME induced by advanced nuclear-burning stages (e.g., Na is produced through oxygen burning and its mass fraction raised in the O-rich shell by a factor of ~ 10 over the solar value in model s15N while in model m15Mdot the sodium mass fraction is 3.4×10^{-5} throughout the ejecta). For IMEs like Ne, Mg, Si, S, or Ca, which are treated explicitly in the approx-21 nuclear network used here (Timmes 1999), the distribution with depth of their mass fraction is comparable for models m15Mdot and s15N.

Turning to the SN II-P radiation properties, we find that the bolometric light curves for model s15N and m15Mdot are analogous (Fig. 7), overlapping closely at early photospheric times and nebular epochs. We have a 25% difference in bolometric flux during the second half of the plateau. Inspecting the photospheric conditions at 90 d after explosion, we find that models m15Mdot and s15N have at that location the same temperature of 5200 K but radii of 2.334×10^{15} cm and 2.589×10^{15} cm, which translates into the 23% offset in bolometric flux. At corresponding ejecta velocities of $\sim 3000 \text{ km s}^{-1}$, the s15N ejecta remains more optically thick, which likely arises from the $\sim 10\%$ larger ^{56}Ni mass and the stronger mixing into the H-rich envelope. The length of the plateaus coincides. More striking is the comparable color evolution followed by each simulation. As we argue in the next section, this largely results from the similar progenitor radii. Finally, the spectral evolution is nearly identical for each model, revealing the same features, with the same strengths and widths at most times. The larger difference is seen at nebular times. The decay energy injection being the same, the spectral differences arise at such late times from the smaller mass of oxygen and sodium (weaker O I and Na I D), sometimes combined with a different species distribution. This is the case for Ca which is more centrally concentrated in

model m15Mdot. This is likely the cause of the weaker Ca II triplet and [Ca II] 7300 Å doublet in model m15Mdot.

This comparison suggests that with the MESA STAR parameters employed to calculate the evolution of model m15Mdot, the final RSG structure and composition are qualitatively and quantitatively similar to the KEPLER model s15 (Woosley & Heger 2007). This also validates the combined approach with MESA STAR and \dot{M} for feeding SN ejecta into CMFGEN. Accounting for sub-dominant species by setting their abundance to the environmental mass fraction also proves to be a suitable approach. The modest contrast we find also shows how degenerate the SN II-P observables are with respect to the pre-SN conditions — the sensitivity to abundance variations is weak for many species. In the next sections, we discuss in detail some dependencies of SN II-P radiation to changes in progenitor and explosions properties.

6 DEPENDENCY ON PROGENITOR RADIUS

To assess the influence of the progenitor radius on SN II-P radiation, we selected models m15mlt1 ($R_{\star} = 1107 R_{\odot}$) and m15mlt3 ($R_{\star} = 501 R_{\odot}$). Models evolved at different metallicity or with enhanced rotation also cover a range of pre-SN star radii too, but they differ in other ways, while models m15mlt1 and m15mlt3 have essentially the same He-core and H-rich envelope mass. Below, we first discuss the CMFGEN predictions for these two models, then compare to SN 1999em observations, before drawing the implications of these results.

6.1 Results for the luminosity, color, and spectral evolution

Owing to its more compact progenitor star, model m15mlt3 is subject to a stronger cooling through expansion. We thus expect to see a smaller plateau luminosity and a more rapid transition to the recombination phase compared to model m15mlt1 (the contrast with model m15mlt2 is present albeit weaker).

Model m15mlt3 indeed produces a genuine plateau in the V -band light curve (one magnitude fainter than the representative brightness in m15mlt1), and a systematic fading in the U -band (fainter by about 2 magnitudes than in model m15mlt1) from the onset of the simulation at 10 d after explosion (top panel of Fig. 8). The onset of the plateau phase (i.e., when T_{phot} drops down to ~ 5500 K, or when the V -band starts to flatten after the explosion) is at ~ 20 d after explosion in m15mlt3 but as much as ~ 45 d in model m15mlt1.

Hence, a factor of two change in progenitor radius produces an interesting morphological change in a SN II-P multi-band light curve, reflecting modestly the stronger trend observed in Type II SN colors arising from compact BSG-star explosions (e.g., SN 1987A, for which CMFGEN does reproduce the U -band fading satisfactorily when the model atoms are complete enough; Dessart & Hillier 2010; Li et al. 2012) and from more extended RSG-star explosions (see, e.g., Brown et al. 2009).

The impact of the progenitor radius on SN II-P radiation is better revealed by inspecting the spectral evolution, from the photospheric to the nebular phase (bottom panel of Fig. 8). Confirming the color evolution discussed above, model m15mlt3 systematically shows a cooler spectrum during the plateau phase, transitioning to the recombination phase about 20 d earlier. This is noticeable through the earlier appearance of Ca II and Fe II lines as well as the weakening of the UV flux, which results from enhanced photospheric cooling and line blanketing. The contrast with model

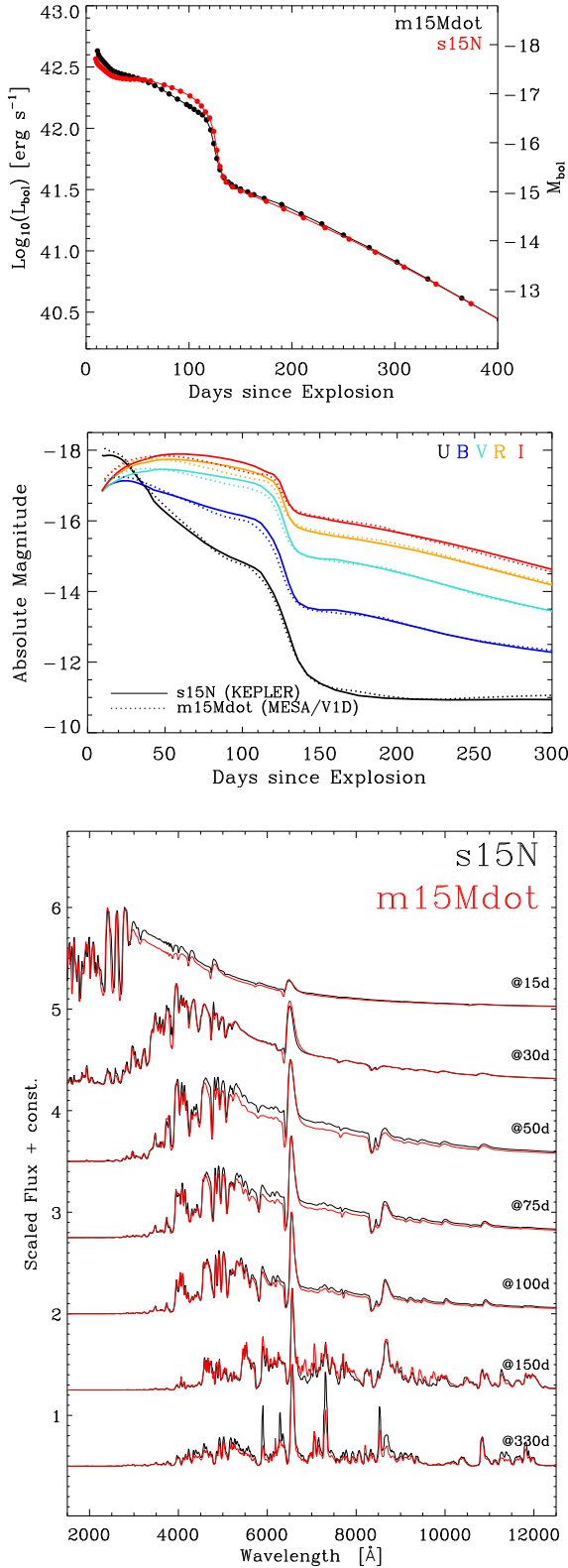


Figure 7. Comparison of CMFGEN results based on a pre-SN and explosion model computed with KEPLER (model s15N) or based on a pre-SN evolution model computed with MESA STAR and exploded with $\dot{\text{I}}\text{d}$ (model m15Mdot). Both models have the same main-sequence mass of $15 M_{\odot}$, but also have similar pre-SN star and ejecta properties (Table 1). We show the bolometric light curves (top), multi-band light curves (middle), and spectral evolution (bottom; spectra are normalized at the redmost wavelength and stacked vertically for clarity).

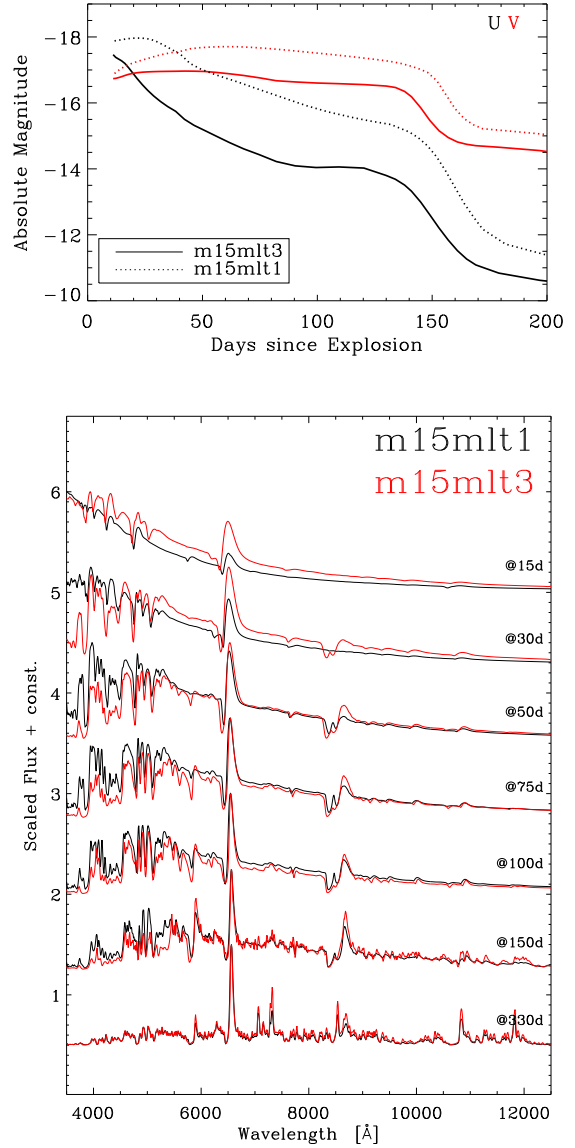


Figure 8. Comparison of the photometric (top) and spectral evolution (bottom) for models m15mlt1 and m15mlt3. Model m15mlt1 corresponds to the explosion of a star with a larger progenitor radius ($R_{\star} = 1110 R_{\odot}$), which results from the smaller adopted mixing-length parameter. Consequently, it has a brighter and bluer plateau, evidenced spectroscopically through the delayed photosphere recombination compared to model m15mlt3 ($R_{\star} = 500 R_{\odot}$), which arose from a more compact progenitor. Having similar cores, they exhibit similar nebular-phase spectra (an offset of $\sim 40\%$ in ^{56}Ni mass leads to a comparable shift in nebular flux level).

m15mlt1 ebbs as time progresses. Leaving aside the 40% difference in absolute flux level between the two (which stems from a 40% difference in ^{56}Ni mass), the nebular phase spectra are essentially identical, i.e., they have the same color, identical lines of a similar width but with a strength that differs by few tens of percent.

A change in progenitor radius therefore affects primarily the plateau phase. The correlations obtained by Litvinova & Nadezhin (1985) suggest a 0.5 mag brighter plateau for our m15mlt1 model

parameters compared to m15mlt3, while we obtain a larger contrast of ~ 1 mag. Our computation of the full spectrum at all times in non-LTE and with large model atoms reveal an important change in color evolution and light-curve morphology. These changes suggest that a smaller progenitor radius may in fact cure the persistent color problem we encounter with models s15O/s15N (Section 2) when comparing to SN II-P light-curve properties.

6.2 Comparison to observations

When comparing model m15mlt3 (model with the smaller progenitor radius and faster cooling/recombination) with the observations of SN 1999em, we find that the agreement is much improved compared to what we obtained previously with model s15N (top-left panel of Fig. 9). The multi-band light curves agree rather well, albeit a slight offset in U and B bands. We have a genuine plateau as observed, although we find that the plateau length in model m15mlt3 is too long. This stems from its large H-rich envelope mass of $10.16 M_{\odot}$, which is $1.5 M_{\odot}$ larger than in models s15N or m15Mdot whose plateau length is on the order of 120 d (in rough agreement with SN 1999em), and from the somewhat larger ^{56}Ni mass of the model ($0.086 M_{\odot}$ in m15mlt3 compared to either the $0.036 M_{\odot}$ inferred by Utrobin (2007) or to the $0.056 M_{\odot}$ inferred by Bersten et al. (2011)).

Spectroscopically, the agreement with observations is better than obtained with model s15N (modulo a time shift at the end of the photospheric phase since the plateau is ~ 30 d longer in model m15mlt3 than observed in SN 1999em). The comparison at 22 d is remarkable (top-right panel of Fig. 9), since it matches in relative flux, in absolute flux, and corresponds to the same post-explosion time of 22 d as inferred for SN 1999em (Dessart & Hillier 2006). During the recombination phase, the agreement is also very good but to match the color we need to take a 13 d older ejecta model (bottom-left panel of Fig. 9). The match at nebular times is excellent (bottom-right panel of Fig. 9), which supports the expectation that the H-rich envelope properties (e.g., its total mass or original extent) have a weaker influence on the nebular-phase properties.

Our model m15mlt3 has properties $E_{\text{kin}} = 1.3 B$, $M_{\text{H-env}} = 10.2 M_{\odot}$ and $R_{\star} = 500 R_{\odot}$. This is in good agreement with the findings of Utrobin (2007). Bersten et al. (2011) find a somewhat larger progenitor radius and argue for extensive ^{56}Ni mixing into the H-rich envelope in order to match the near-constant plateau luminosity. These two works quote ejecta masses but what these truly model is the H-rich envelope mass, which in both works is on the order of $10 M_{\odot}$. We stress again that the plateau light curve sets a meaningful constraint on the H-rich envelope properties (including its mass), but provides no information on the He-core mass. Determining the total *ejecta* mass requires the additional modeling of the nebular spectra to infer the oxygen and calcium masses (Li & McCray 1992, 1993; Jerkstrand et al. 2012), and helium-core kinematics (Dessart et al. 2010a).

6.3 Implications

The only simulations in our grid (Table 1) that show a systematic fading in the U -band light curve are models m15mlt3 and m15z2m3, which both have a progenitor radius of $\sim 500 R_{\odot}$. All other simulations, characterized by larger progenitor radii between 600 – $1100 R_{\odot}$, exhibit a U -band plateau before fading, or even a bump for the largest progenitor stars. Our results thus indicate that in order to match the color evolution of SNe II-P, progenitor radii on the order of $\sim 500 R_{\odot}$ may be required.

This seems incompatible with the inferences of RSG stars in the Galaxy and in the Magellanic clouds (Levesque et al. 2005, 2010). Indeed, it is generally thought that RSG stars are very extended stars, with radii even as large as $1500 R_{\odot}$. This notion is supported by interferometric observations of nearby RSG stars, yielding photospheric radii of $\sim 950 R_{\odot}$ for Betelgeuse (Haubois et al. 2009; Neilson et al. 2011), and as much as $1420 R_{\odot}$ for VY CMa (Wittkowski et al. 2012). It is important, however, to realize that the RSG radius we constrain from SN II-P radiation modeling is the radius that contains the bulk of the mass. Photometric and spectroscopic observations of RSGs reveal instead the location where the photons decouple from the atmosphere, which corresponds to an optical-depth at that wavelength of $2/3$. Unfortunately, there is ample evidence that these two radii do not coincide in RSGs, and that the situation is complicated further by the inherent uncertainties associated with stellar evolution/structure and stellar atmosphere calculations.

As we demonstrate in Section 3, varying the mixing length parameter can dramatically alter the radius of the stellar model, i.e., the location where the Rosseland mean optical depth would be $2/3$. This property is well known (see, e.g., Maeder & Meynet 1987) and implies that stellar evolutionary models predict the RSG luminosity but make no reliable prediction about the surface radius and effective temperature. By varying the mixing length parameter, one can produce a huge range of RSG radii, without impacting the RSG luminosity or the helium-core properties. Experimenting with MESA STAR, we have produced $15 M_{\odot}$ models that die as RSGs with radii of $2500 R_{\odot}$ ($\alpha = 0.1$) down to $350 R_{\odot}$ ($\alpha = 5$), all with $\log(L/L_{\odot}) = 4.8$. Note that for increasing convective fluxes, the convective motions become eventually supersonic, requiring a multi-dimensional and hydrodynamical treatment. Such supersonic motions are in fact inferred in RSG atmospheres (Josselin & Plez 2007).

The observational side is also problematic. Recently, using both optical and near IR ranges, Davies et al. (2013) have modeled the spectral energy distribution of RSG stars and found that these objects are much warmer than previously inferred, in particular through optical analyses alone (Levesque et al. 2005). This revision of RSG effective temperatures leads to a reduction of RSG radii by as much as 20–30%. Furthermore, convection, molecule and dust formation, as well as time-dependent mass loss rates complicate considerably the inference of a meaningful $\tau = 2/3$ surface. Its location is function of the effective opacity of the medium, which varies with wavelength, and the atmospheric structure (density scale height for example). It is thus unclear how that surface, located somewhere within the outer $\sim 10^{-5} M_{\odot}$ may relate to the radius that contains the bulk of the RSG mass.

Finally, as already discussed in Section 3, a fundamental property of RSG H-rich envelopes is their low binding energy. This implies that little work is needed to modify their structure, and in particular their extent. For example, VY CMa is characterized by a huge radius, but it is also known to have an extremely intense mass loss history (Decin et al. 2006). If it were to explode today, it would probably be classified not as a SN II-P, but more probably as a SN IIn (Smith et al. 2009), or as a SN II-Linear. Phases of intense mass loss in RSGs may be associated with a surface phenomenon, e.g., pulsations or some other mass loss mechanism (Yoon & Cantiello 2010). But alternatively, the envelope may be reacting to the strengthening of shell burning at the edge or within the helium core, or to the emergence of acoustic/gravity waves excited by convection deep in the star (Quataert & Shiode 2012). In other words, the extreme radii of such RSG stars that we measure

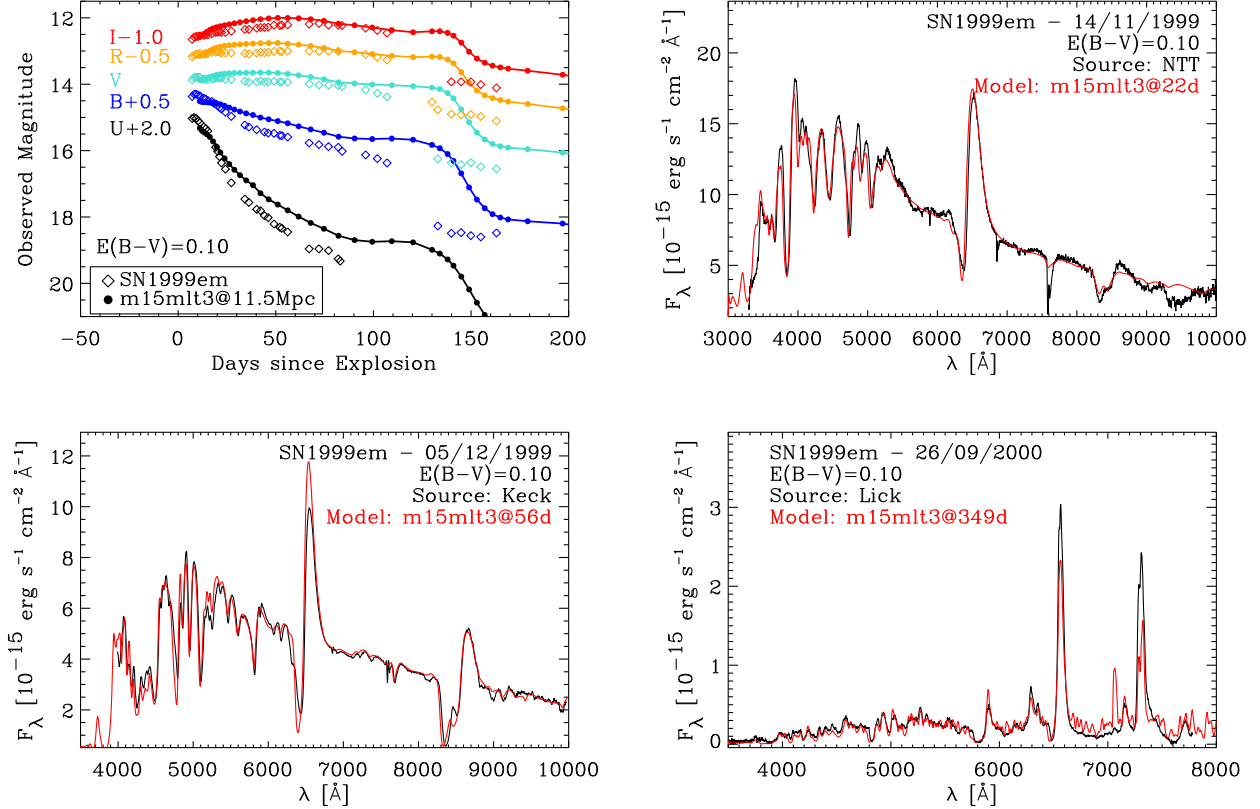


Figure 9. Comparison between the observations of SN1999em and model m15mlt3 (these results should be compared with those for model s15N shown in Figs. 3–4), which arises from a more compact RSG star ($R_* = 500 R_\odot$) than model s15N ($R_* = 810 R_\odot$). The larger H-rich envelope mass produces a longer plateau than observed (something easily corrected for if we invoke a smaller mass RSG or stronger mass loss) while other synthetic signatures match the SN 1999em multi-band light curves and spectra simultaneously.

today may results from processes that are ignored in current stellar-evolution codes, which assume a quasi-hydrostatic, 1-D, stellar structure.

The strong sensitivity of SN II-P radiation to progenitor radius makes it a valuable probe of the pre-SN structure. It represents a useful observable to constrain RSG “mass-radii” (that same quantity coming out of stellar-evolution calculations), potentially more reliable than interferometric or spectroscopic/photometric measurements on RSG atmospheres which constrain an ambiguous, time-dependent, wavelength dependent, mass-loss rate dependent “ τ -radius”.

7 DEPENDENCY ON CORE OVERSHOOTING

As discussed in Section 3, increasing the efficiency of core overshooting in a $15 M_\odot$ star has the primary effect of increasing the helium core size, while the associated increase in luminosity and mass loss leads to a reduction of the total star mass at death. In our simulations, the original surface chemistry is mildly altered, typically at the few percent level for intermediate mass elements. We note, however, that in the case of strong core-overshooting, the RSG surface chemistry might reflect instead the influence of the CNO cycle operating in the core, with Helium enhanced by a few percent, Nitrogen increased by a factor of ~ 4 , while C and O mass fractions are decreased by a few 10%. Here, the main impact

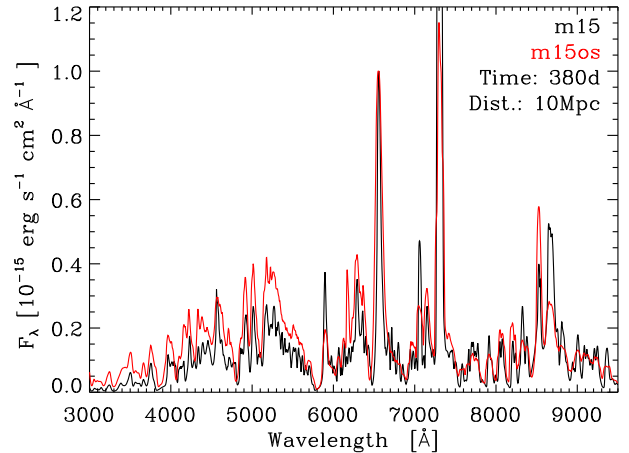


Figure 10. Comparison between synthetic spectra for models m15 and m15os at 380 d after explosion. The m15os flux is normalized to that of model m15 at 6560 Å.

of enhancing core overshooting is to make a star act as if it was more massive, and thus bears a similar impact to stellar rotation (Maeder & Meynet 2000).

Using radiation hydrodynamics simulations of RSG star explosions, Dessart et al. (2010a) demonstrated that the velocity at the junction between the He core and the H envelope is a critical

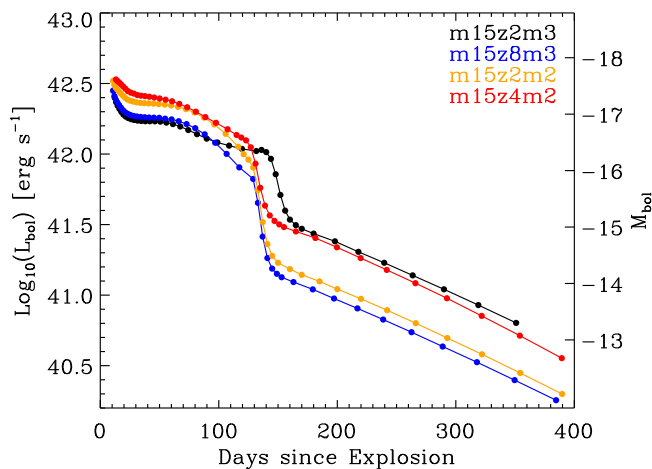


Figure 11. Bolometric light curves for the m15 series for different progenitor metallicities, from a tenth to twice the solar value. See Table 1 for details.

marker of the pre-SN star. They find that in order to reproduce the typical observed width of the O I 6300 Å fine-structure line or H α , the outer edge of the He core or the inner edge of the H-rich envelope in the progenitor must be expelled at velocities on the order of $\sim 1500 \text{ km s}^{-1}$. In turn, this implies a progenitor star of $\lesssim 20 M_{\odot}$, because higher mass stars would place that junction at higher velocities (for the same standard explosion energy). They note that if stellar rotation is allowed for, it pushes this limit to lower main-sequence masses. Since overshooting and rotation cause the same basic effect on the He-core mass, enhanced overshooting will lower that mass limit of SN II-P progenitors to lower values than the estimated $\sim 20 M_{\odot}$ (Dessart et al. 2010a; Jerkstrand et al. 2012).

Inferences about the core are best done at nebular times, when the radiation comes from ejecta regions that used to reside in the He-core and at the base of the H-rich envelope. In our synthetic spectra for model m15 and m15os (Fig. 10), we find that the typical half-width-at-half-maximum (HWHM) of H α is 2500 km s^{-1} in model m15os and only $\sim 1000 \text{ km s}^{-1}$ in model m15. These values are close to the ejecta velocity we measure at the junction between H-rich and He-rich shells, which are 2500 and 1500 km s^{-1} for models m15os and m15, respectively. Given the similar ejecta kinetic energy of 1.4 and $1.27 B$ for these models, the difference stems in part from the contrast in $M_{\text{ejecta}}/M_{\text{He core}}$ ratio.

We note that the greater ^{56}Ni mass synthesized in model m15os probably contributes to making the HWHM of H α larger. In both models, the Doppler velocity at maximum absorption in H α is located within the H-rich ejecta shells, as 3800 and 5300 km s^{-1} , both larger than observed in SN 1999em. Getting the profile absorption of H α “right” is however a recurrent problem, even at photospheric times, because the line is so sensitive to even subtle changes in ionization.

To summarize, core overshooting increases the uncertainty when inferring the mass of a SN II-P progenitor, because, like rotation, it makes the star evolve as if it was more massive but unaffected by overshooting.

8 DEPENDENCY ON METALLICITY

The impact of metallicity on SN II-P radiation can be split into two categories. First, metallicity is a key ingredient affecting pre-

SN evolution. It may be a source of under-abundant elements for nuclear reactions. Its influence on opacity, in particular through variations in iron abundance, can cause the envelope to shrink or expand because radiative diffusion in the envelope controls in part the radius of the star. But more importantly, it can modulate the stellar-wind mass loss rate and thus result in pre-SN stars of varying masses. Metallicity is critical here because it provides the necessary species for molecule and dust formation in cool stars, and ions with optically-thick lines in hotter stars (Castor et al. 1975). In their respective environments, each opacity source is key for driving a stellar wind.

Second, metallicity will directly influence SN II-P spectra and colors. Indeed, metals, even at solar metallicity, play a critical blanketing role on the photospheric flux, blocking the flux at specific wavelengths or over wide spectral regions through line overlap. Hence, metallicity has the potential to alter the color as well as the line-profile signatures of SNe II-P. Through its effect on pre-SN mass loss and the H-rich envelope mass, varying metallicities should lead to a range of ejecta masses of SNe II-P in different environments, influencing in particular the length of the plateau phase.

We expect all these effects to play a role in SN II-P properties but it is unclear today if we have seen such metallicity effects. The main impediment is the wide-spread use, only starting to change now, of targeted surveys, which focus on similar types of galaxies and thus deliver a restricted view of the diversity of SNe in our Universe. Below, we discuss what distinctive signatures we expect from SNe II-P at different metallicities.

With MESA STAR, we have run simulations for a $15 M_{\odot}$ star at metallicities of 0.002 (model m15z2m3; one tenth solar), 0.008 (m15z8m3), 0.02 (m15; our reference model, also called m15z2m2), and 0.04 (m15z4m2). We find that at lower metallicity, the lower mass-loss rates produce higher mass stars at the time of death, while the reduced H-rich envelope opacity (dominated by contributions from electron scattering and metal lines) produces smaller radii (Table 1). Consequently, the cooling from SN expansion is modulated, producing a fainter plateau and a faster color evolution for lower-metallicity SNe II-P. The lower envelope masses at higher metallicity, on the other end, produce a SN II-P with a shorter plateau. Finally, the varying ^{56}Ni masses synthesized in the explosion introduce a range of nebular-phase luminosities (Fig. 11). By themselves, these properties do not set any constraint on the metallicity because they could stem from different convection efficiencies affecting the progenitor radius, or different mass-loss rates peeling differentially the H-rich envelope. Unambiguous metallicity signatures are to be found instead in SN II-P spectra.

For as long as the SN II-P photosphere is in the outer parts of the H envelope (which holds for typically half the photospheric phase; Dessart & Hillier 2011), the spectrum formation region is located in shells that have the metallicity at which the star formed, thus unaffected by nuclear burning in the course of the evolution and explosion, or by mixing following explosion. If mixing occurs during the pre-SN evolution, ashes from the CNO cycle may pollute the outer progenitor envelope, but we find that apart from a sizeable impact on nitrogen, other species are unaffected (e.g., H, He) or only mildly affected (e.g., C and O, at the few tens of percent level). This is to be contrasted with the potential variation of *all* metal abundances by a factor of a few if the SN is located in sub-solar or super-solar metallicity environments.

To best reveal the influence of metallicity on the spectra, without being affected by the different cooling rates of the associated ejecta, we compare SN II-P simulations m15z2m3, m15z8m3, m15z2m2 (our reference model), and m15z4m2 when they have the

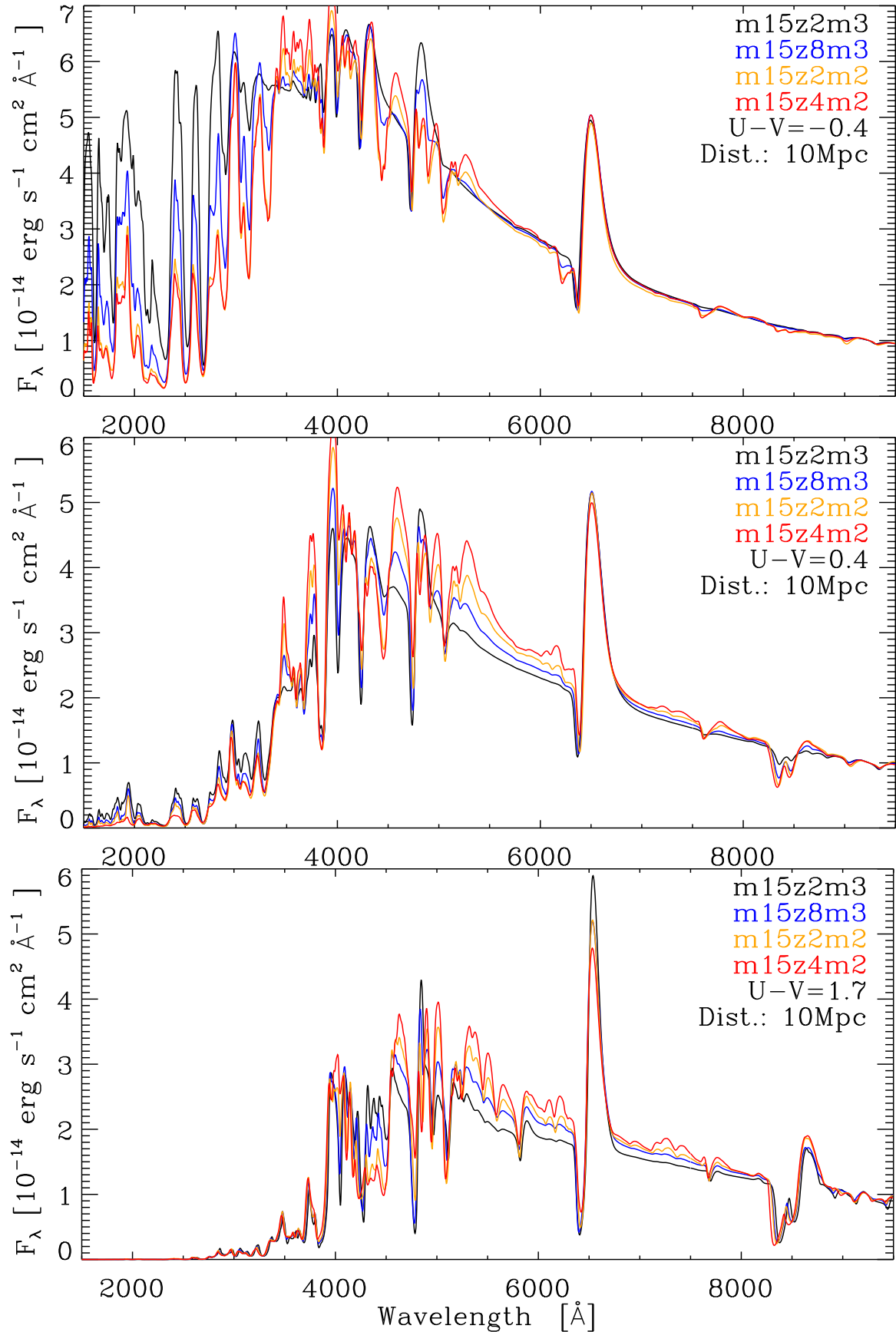


Figure 12. Comparison of synthetic spectra at selected $U - V$ colors for SNe II-P arising from a $15 M_\odot$ progenitor evolved with different initial metallicities, from sub-solar (model m15z2m3) to super-solar (model m15z4m2) — see Table 1. Because the color evolution is different for each model, these correspond to different post-explosion times. When $U - V = -0.4$, the SN ages are 17.1, 19.1, 22.1, and 22.9 d for models m15z2m3, m15z8m3, m15z2m2, and m15z4m2. In the same model order and when $U - V = 0.4$, the SN ages are 30.2, 30.7, 33.7, and 31.0 d, while when $U - V = 1.7$, the SN ages are 80.2, 66.0, 72.6, and 63.3 d.

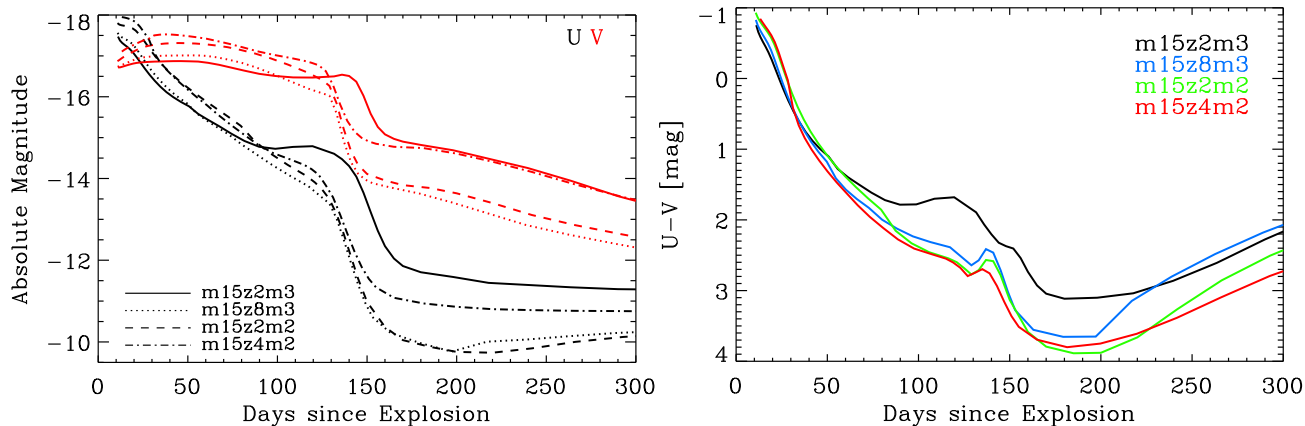


Figure 13. *Left:* U and V -band light curves for models m15z2m3, m15z8m3, m15z2m2, and m15z4m2. *Right:* Evolution of the $U - V$ color.

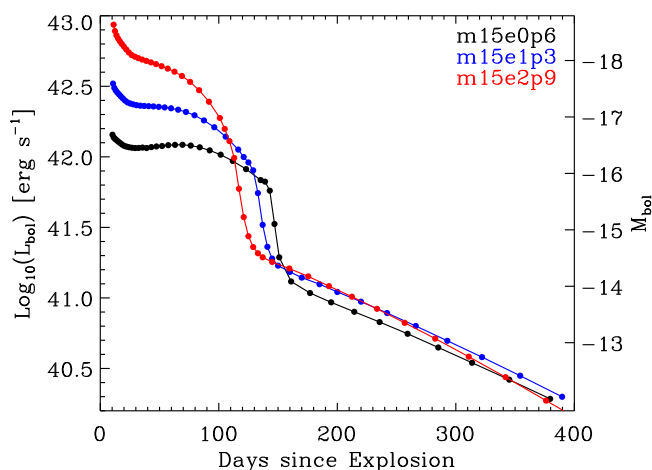


Figure 14. Bolometric light curves for the reference model m15 but exploded to produce ejecta kinetic energies of 0.6, 1.3, and 2.9 B (models m15e0p6, m15e1p3, and m15e2p9, respectively).

same $U - V$ color. This ensures that we are comparing the spectra when their photospheric (or color) temperatures are similar. An observer can make a similar comparison when the time of explosion is not known — the reddening must, however, be known. In Fig. 12, we show snapshots at three different epochs corresponding to $U - V$ of -0.4 , $+0.4$, and $+1.7$ mag (the corresponding post-explosion times in each case are given in the figure caption).

At early times ($U - V = -0.4$), the influence of metallicity is strong throughout the spectrum. In the UV, the flux level is significantly enhanced at lower Z , owing to the reduction of line blanketing, and in the optical, metal lines appear much weaker. Since all species other than H and He are at the environmental metallicity, we observe an effect in lines associated with O, Sc, Si, and Fe. As the ejecta recombines ($U - V = 0.4$), the flux level in the UV becomes insensitive to metallicity variations (probably because of a saturation in line absorption and a reduction in gas emissivity at UV wavelengths), and the contrast in the optical is as strong as before, but is now also apparent in Ca lines (Ca II H&K as well as the triplet at 8500 \AA) — $H\alpha$ hardly changes between models at those times. Nearer the end of the plateau phase, the UV flux is identical amongst these models. Differences in the optical are caused primarily by Ti II (around $4000\text{-}4500 \text{ \AA}$) and Fe II lines (model m15z2m3 shows very weak Fe II lines). Individual lines like

Na I D or O I 7770 \AA reveal the systematic abundance difference between models.

Comparing the multi-band light curves for models m15z2m3, m15z8m3, m15z2m2, and m15z4m2 is difficult because they differ not just in metallicity but also in progenitor radii (from ~ 500 to $\sim 800 R_{\odot}$; resulting from the different envelope opacity) and ^{56}Ni mass (~ 0.04 to $\sim 0.09 M_{\odot}$; inherent to the way the piston-driven ejecta was produced). Although lower metallicity models suffer less blanketing in the UV and should appear bluer, the effect is compensated by their lower progenitor radii that cause stronger cooling through expansion and hence cooler photospheres (Fig. 13). Identifying a metallicity effect in the color evolution is thus non trivial, in particular compared to the ease with which we find metallicity-dependent signatures in the spectra (Fig. 12). Although detailed modeling specifically tailored for SN 1999em will be needed, the strength of lines from IMEs and IGEs in the spectra of SN 1999em, and the good agreement with the solar-metallicity model m15mlt3 shown in Fig. 9 (see also synthetic fits in Dessart & Hillier 2006, 2011) suggest that the metallicity of the progenitor star may be solar. Hence, our models do not support a one-fifth-solar metallicity for SN 1999em, as suggested by Baklanov et al. (2005).

The interesting result from this exploration is that SNe II-P show signs of differing metallicities not just in lines of Fe, but also in lines of O, Na, Sc, Ti, or Ca, and can thus provide a much richer assessment of metallicity variations than, e.g., nebular-line analyses, which focus primarily on oxygen abundances. Being so luminous, one may use SN II-P spectra to determine the SN metallicity, which is critical to infer the influence of metallicity on pre-SN evolution. Importantly, we are measuring the metallicity of the SN rather than a mean metallicity of the galaxy or the SN environment.

9 DEPENDENCIES ON EJECTA KINETIC ENERGY

In this last section, we explore the dependency of SN II-P radiation on explosion energy employing our reference m15 model for starting conditions. For clarity, we refer to this reference model as m15e1p3, to specify its kinetic energy of 1.27 B. We ran two additional models exploded to yield an ejecta kinetic energy of 0.6 B (model m15e0p6) and 2.9 B (model m15e2p9).

A larger explosion energy yields a brighter and shorter plateau. Conversely, a smaller explosion energy yields a fainter and longer plateau. Halfway through its photospheric phase, model

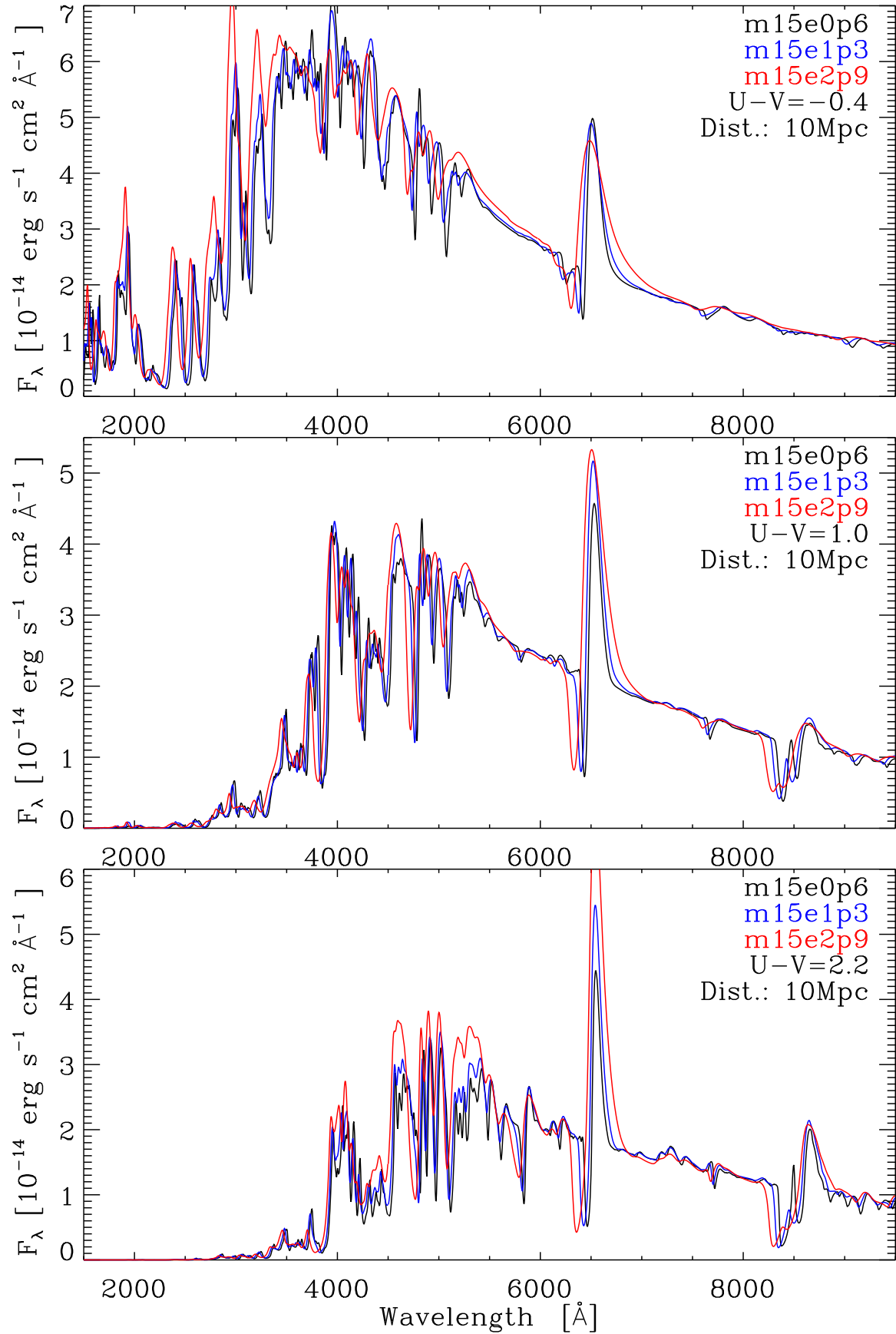


Figure 15. Spectral comparison at selected $U - V$ colors for the reference model m15 but exploded to produce ejecta kinetic energies of 0.6, 1.3, and 2.9 B (models m15e0p6, m15e1p3, and m15e2p9, respectively). The bolometric light curves for these models are presented in Fig. 14. Each comparison corresponds to contemporaneous post-explosion times because all models have essentially the same color at a given post-explosion time.

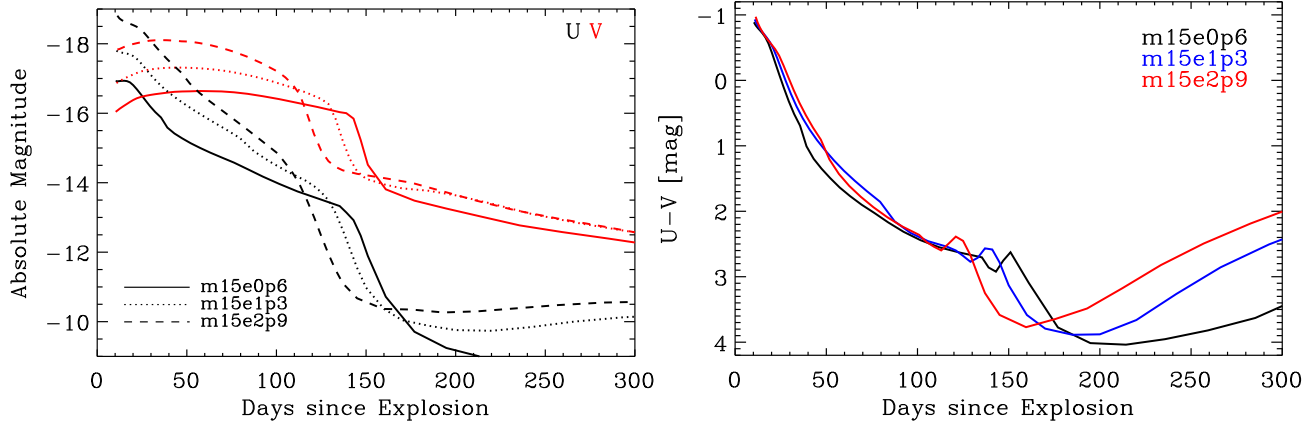


Figure 16. *Left:* U and V -band light curves for models m15e0p6, m15e1p3, and m15e2p9. *Right:* Evolution of the $U - V$ color. Notice the strong degeneracy between models at photospheric epochs.

m15e2p9 is 1.35 mag brighter in V than model m15e0p6, which is close to the 1.5 mag contrast predicted by the correlations of Litvinova & Nadezhin (1985) for the corresponding model parameters. Also, more ^{56}Ni is synthesized in higher-energy explosions which translates into a stronger nebular flux (Fig. 14). Faster expansion in the H-rich envelope leads to broader lines during the photospheric phase. Photospheric velocity measurements at mid-plateau phase can in fact provide a fair assessment of the ejecta kinetic energy (Dessart et al. 2010a). Interestingly, our models suggest that SN II-P color evolution is independent of explosion energy. For example, we show a spectral comparison at three epochs in Fig. 15, corresponding to $U - V = -0.4, 1,$ and 2 mag, and find that each correspond to the same post-explosion date to within a few days at most. This degenerate color evolution is shown in Fig. 16. While there is an obvious shift in absolute magnitude reflecting the different radii of the photosphere for each model (left panel), the $U - V$ color is the same at a given post-explosion date for all models during the photospheric phase. This property is somewhat coincidental. The energy deposited by the shock corresponds to a representative expansion rate (considering a given ejecta mass). And, the greater the shock-deposited energy, the greater the cooling from the subsequent expansion. Higher energy explosions start with a larger ejecta temperature, but that energy is degraded more strongly the faster the ejecta expands (for an adiabatic evolution, we have $T \propto 1/R$).

As a last illustration, we show in Fig. 17 the correspondence between model m15e0p6 and the under-luminous SN 2005cs (Pastorello et al. 2006; Brown et al. 2007; Dessart et al. 2008). It is not the scope of the present work to provide a detailed analysis of that SN. However, we see that our model m15e0p6 provides a satisfactory match to the observations during the photospheric phase (line widths and strengths, colors). At nebular times, the comparison is less satisfactory. Our model is too luminous (our ejecta model has initially $0.046 M_{\odot}$ of ^{56}Ni when $\sim 0.008 M_{\odot}$ was inferred by Utrobin & Chugai 2008) and shows broader lines than observed for Na I D or $\text{H}\alpha$. As before, $\text{He I } 7065 \text{ \AA}$ is too strong. However, the slower expansion rate of this ejecta shows clearly the P-Cygni profile associated with the K I resonance line at $7664\text{--}7698 \text{ \AA}$.

Hence, from the restricted exploration performed in this paper, the diversity in color evolution of SNe II-P is found to stem not from different explosion energies but primarily from different progenitor radii.

10 SUMMARY AND OUTLOOK

We have presented a set of simulations for the evolution of a massive star, the explosion that follows core collapse, and the evolution of the radiation of the resulting supernova. Our goal is to connect the SN radiation properties with physical processes affecting stellar evolution and the explosion, and build a consistent picture encompassing all relevant aspects. This is important because determining the pre-SN star mass provides only a lower limit on the main-sequence star mass, and no information on the processes that make the two differ. Determining the H-rich envelope mass from the bolometric light curve places no constraint on the Helium core mass, which is in fact a much more reliable tracer of the main-sequence mass (Dessart et al. 2010a). A consistent picture of SN explosions must attempt to address not just the progenitor mass, but also the role of rotation, convection/overshooting, metallicity etc. on the evolution of a star until core collapse, and thus tackling these issues from first principles is a sensible goal.

We have reported on two distinct efforts. First, we revisited the simulations of Dessart & Hillier (2011) to identify the origin of the discrepancies with the observations of the standard SN II-P 1999em. This has proven successful with our upgraded simulations including larger model atoms for Fe I and Fe II, together with the treatment of non-thermal processes and non-local energy deposition. However, a color problem remains (model is too blue for too long), which all attempts at improving the quality of the radiative transfer have failed to resolve fully.

The second effort has been to explore what variation in progenitor and explosion properties could cure this color problem. Using a grid of simulations for a $15 M_{\odot}$ main sequence star calculated with MESA STAR, we study the dependency of pre-SN star properties on mixing length parameter, rotation, overshooting, and metallicity. Variations in these parameters alter global quantities (e.g., the progenitor radius, the H-rich envelope mass, the ratio of H-rich envelope (or ejecta) mass to the helium-core mass), which influence significantly the synthetic SN II-P light curves, although the same main-sequence mass and the same ejecta kinetic energy characterize these simulations. This confirms the difficulty of associating a given SN II-P with a main-sequence progenitor star.

We have also compared the results of MESA STAR with those obtained by KEPLER. With a suitable (and sensible) choice of parameters, both codes produce a similar pre-SN star from a $15 M_{\odot}$ star on the main sequence. The resulting explosions for these KE-

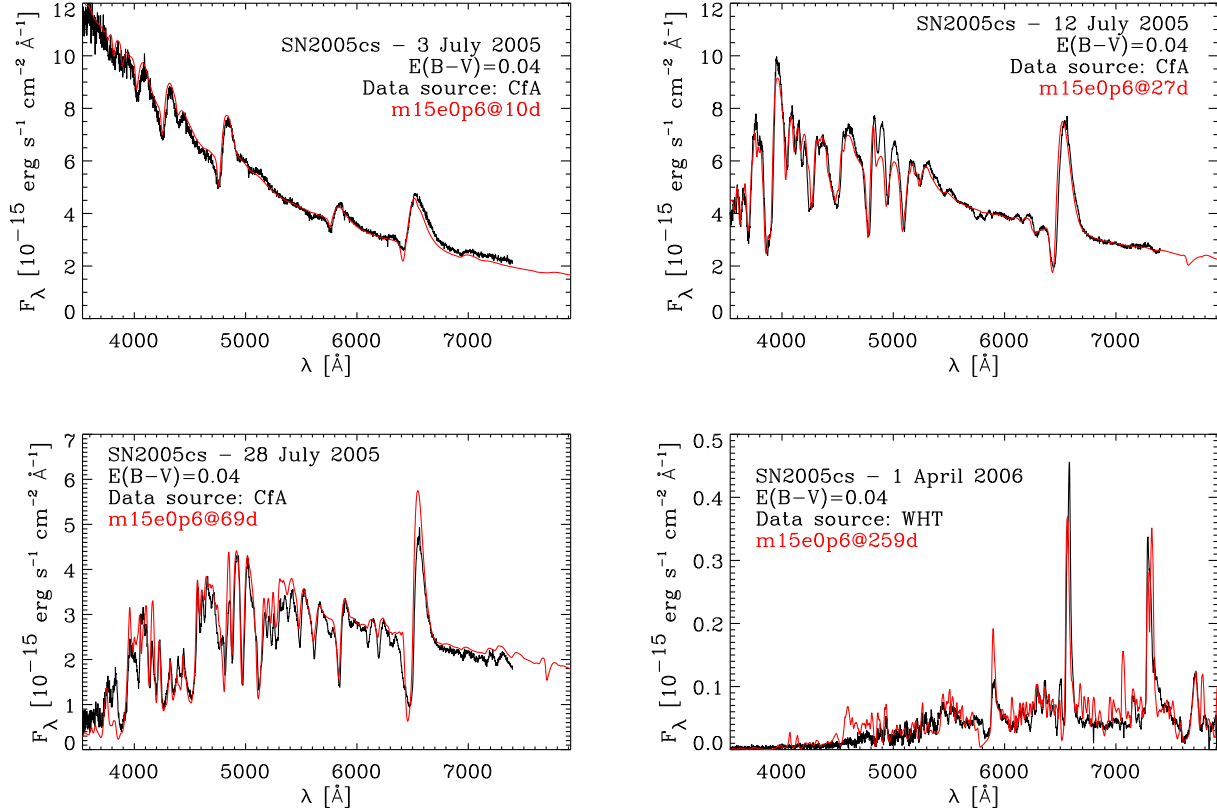


Figure 17. Spectral comparison between SN 2005cs (Dessart et al. 2008) and the under-energetic model m15e0p6 (the synthetic spectra are first reddened with $E(B - V) = 0.04$ mag and later normalized to observations at 6000 \AA). In this illustration, we are merely interested in comparing the relative agreement between model and observations when the colors match — the absolute flux level, which may be offset due to an inadequate explosion energy, progenitor radius, or ^{56}Ni mass, is not of primary interest here. This agreement suggests we are modeling satisfactorily the radiative transfer in the photospheric layers.

PLER and MESA STAR pre-SN star models yield comparable LCs and spectra. The specific case we describe highlights the degeneracy of SN II-P radiation — strong variations in mixing and chemical composition in sub-dominant species are associated with only modest variations in observables.

In the MESA STAR exploration, the most interesting result is obtained with the $15 M_{\odot}$ models evolved using different mixing length parameters. All else being the same (opacities, mass, metallicity etc), more efficient convection yields more compact RSG stars. This change does not affect other stellar properties at death, such as total mass or helium core mass. We find that the reduction of the progenitor radius from $800 R_{\odot}$ to $500 R_{\odot}$ cures nearly completely the color problem identified in all our SN II-P simulations. Independent of our work and diagnostics, recent radiative-transfer calculations of RSG atmospheres propose a systematic reduction of RSG radii (Davies et al. 2013). One may argue that very extended RSG stars exist. However, these RSGs often exhibit intense mass loss episodes, as in the case of VY CMa. If it were to explode, rather than producing a type II-P, the resulting SN would probably be a Type II_n, or a II-L.

The effect of metallicity is interesting. It is visible in the pre-SN object through the influence on the final mass and radius. In the SN II-P spectra, variations in metallicity modulate the magnitude of line blanketing, which affects the entire UV range. In the optical, the effect is visible through strong individual line features for numerous metal species, including O, Na, Ca, Ti, and Fe. Hence,

the outer layers of SN II-P ejecta, unaffected by steady/explosive burning or mixing, represent a great potential for metallicity studies. SN II-P observations could be used to infer the metallicity at the SN site, which is important to understand the progenitor evolution, but also as a tool to infer metallicities in the nearby and distant Universe. This may prove particularly useful in the coming years with JWST and extremely large telescopes.

The influence of kinetic energy corroborates previous findings, more energetic explosions yielding a brighter and shorter plateau while the larger explosion energy produces broader spectral lines at all times. We find that the SN color evolution is independent of explosion energy, i.e. the SN exhibits the same color at a given post-explosion date irrespective of explosion energy. This suggests that, at a given metallicity, the main factor affecting SN II-P colors is the progenitor radius. We note that SNe II-P will systematically evolve from high to low (recombination) temperatures and will therefore step through the same spectral morphology (in the UV or in the optical). It is the *rate* at which their color evolves that will differ between SNe II-P, i.e., being faster in more compact RSGs than in more extended ones.

Since SN II-P light curves are only weakly dependent on the helium core mass, they cannot be used to infer the total ejecta mass. Instead, they constrain the H-rich envelope mass. In hydrodynamical simulations of SNe II-P, this distinction is often missing because, instead of using physically-consistent stellar-evolution models, a simple power law or a polytrope is adopted for the progen-

itor density structure (Litvinova & Nadezhin 1983; Utrobin 2007; Bersten et al. 2011). Such approximated models tend to have a different surface scale height. Furthermore, the Lagrangian mass for the edge of the helium core is arbitrarily positioned. In stellar evolutionary calculations, this edge (which corresponds to the base of the H-rich envelope), is not arbitrarily located, but is instead a very stiff function of main-sequence mass (influenced as well by rotation or core-overshooting). The RSG progenitor envelope thus reveals a highly-bound helium core and a loosely-bound hydrogen-rich envelope. The mass contained in the helium core, which can be large for higher mass progenitors and the corresponding SN ejecta, influences nebular spectral properties but not the light curve.

These issues are in part illustrated by our models computed with rotation and overshooting. Both effects tend to make a given main-sequence star evolve as if it was more massive. For a $15 M_{\odot}$ progenitor, rotation and/or overshooting produce a star at death that has a bigger helium core, has a higher luminosity, is more extended (bigger radius), has suffered strong mass loss (lighter H-rich envelope). In such stars, the helium core contributes a greater fraction of the total ejecta mass, at the expense of the H-rich envelope mass. However, only the latter is constrained from light-curve modeling. Much of the mass discrepancy for SN II-P progenitors today stems from the ambiguity of what is meant by ejecta/progenitor mass. Inferences based on pre-explosion images are fundamentally tied to the star luminosity and thus to the (helium) core mass. In contrast, in the often-adopted formalism of Litvinova & Nadezhin (1983), the “mass” corresponds to the material affecting the plateau light curve, and that mass is the H-rich envelope mass in the progenitor star.

In the future, we will experiment with MESA STAR, $\dot{\Gamma}$ d, and CMFGEN to produce ejecta models whose computed SN light curves and spectral evolution, at both photospheric and nebular times, are compatible with well observed SNe II-P.

ACKNOWLEDGMENTS

LD acknowledges financial support from the European Community through an International Re-integration Grant, under grant number PIRG04-GA-2008-239184, and from “Agence Nationale de la Recherche” grant ANR-2011-Blanc-SIMI-5-6-007-01. DJH acknowledges support from STScI theory grants HST-AR-11756.01.A and HST-AR-12640.01, and NASA theory grant NNX10AC80G. This work was granted access to the HPC resources of CINES under the allocation 2011–c2011046608 and c2012046608 made by GENCI (Grand Equipement National de Calcul Intensif). A subset of the computations were also performed at Caltech’s Center for Advanced Computing Research on the cluster Zwicky funded through NSF grant no. PHY-0960291 and the Sherman Fairchild Foundation.

APPENDIX A:

Illustration of line features at photospheric and nebular times in a SN II-P

APPENDIX B:

Multi-band light curves for the SN II-P models discussed in the main body of the paper.

REFERENCES

- Arcavi, I., Gal-Yam, A., Kasliwal, M. M., Quimby, R. M., Ofek, E. O., Kulkarni, S. R., Nugent, P. E., Cenko, S. B., Bloom, J. S., Sullivan, M., Howell, D. A., Poznanski, D., Filippenko, A. V., Law, N., Hook, I., Jönsson, J., Blake, S., Cooke, J., Dekany, R., Rahmer, G., Hale, D., Smith, R., Zolkower, J., Velur, V., Walters, R., Henning, J., Bui, K., McKenna, D., & Jacobsen, J. 2010, *ApJ*, 721, 777
- Baklanov, P. V., Blinnikov, S. I., & Pavlyuk, N. N. 2005, *Astronomy Letters*, 31, 429
- Bersten, M. C., Benvenuto, O., & Hamuy, M. 2011, *ApJ*, 729, 61
- Bersten, M. C. & Hamuy, M. 2009, *ApJ*, 701, 200
- Blinnikov, S. I., Eastman, R., Bartunov, O. S., Popolitov, V. A., & Woosley, S. E. 1998, *ApJ*, 496, 454
- Brott, I., de Mink, S. E., Cantiello, M., Langer, N., de Koter, A., Evans, C. J., Hunter, I., Trundle, C., & Vink, J. S. 2011, *A&A*, 530, A115
- Brown, P. J., Dessart, L., Holland, S. T., Immler, S., Landsman, W., Blondin, S., Blustin, A. J., Breeveld, A., Dewangan, G. C., Gehrels, N., Hutchins, R. B., Kirshner, R. P., Mason, K. O., Mazzali, P. A., Milne, P., Modjaz, M., & Roming, P. W. A. 2007, *ApJ*, 659, 1488
- Brown, P. J., Holland, S. T., Immler, S., Milne, P., Roming, P. W. A., Gehrels, N., Nousek, J., Panagia, N., Still, M., & Vanden Berk, D. 2009, *AJ*, 137, 4517
- Cardelli, J. A., Clayton, G. C., & Mathis, J. S. 1988, *ApJL*, 329, L33
- Castor, J. I., Abbott, D. C., & Klein, R. I. 1975, *ApJ*, 195, 157
- Chornock, R., Filippenko, A. V., Li, W., & Silverman, J. M. 2010, *ApJ*, 713, 1363
- Davies, B., Kudritzki, R.-P., Plez, B., Trager, S., Lançon, A., Gazak, Z., Bergemann, M., Evans, C., & Chiavassa, A. 2013, *ApJ*, 767, 3
- Decin, L., Hony, S., de Koter, A., Justtanont, K., Tielens, A. G. G. M., & Waters, L. B. F. M. 2006, *A&A*, 456, 549
- Dessart, L., Blondin, S., Brown, P. J., Hicken, M., Hillier, D. J., Holland, S. T., Immler, S., Kirshner, R. P., Milne, P., Modjaz, M., & Roming, P. W. A. 2008, *ApJ*, 675, 644
- Dessart, L. & Hillier, D. J. 2005, *A&A*, 437, 667
- . 2006, *A&A*, 447, 691
- . 2008a, *MNRAS*, 383, 57
- . 2008b, *MNRAS*, 383, 57
- . 2010, *MNRAS*, 405, 2141
- . 2011, *MNRAS*, 410, 1739
- Dessart, L., Hillier, D. J., Li, C., & Woosley, S. 2012, *MNRAS*, 424, 2139
- Dessart, L., Livne, E., & Waldman, R. 2010a, *MNRAS*, 408, 827
- . 2010b, *MNRAS*, 405, 2113
- Dessart, L., Waldman, R., Livne, E., Hillier, D. J., & Blondin, S. 2013, *MNRAS*, 428, 3227
- Eastman, R. G., Woosley, S. E., Weaver, T. A., & Pinto, P. A. 1994, *ApJ*, 430, 300
- Falk, S. W. & Arnett, W. D. 1977, *ApJS*, 33, 515
- Gezari, S., Dessart, L., Basa, S., Martin, D. C., Neill, J. D., Woosley, S. E., Hillier, D. J., Bazin, G., Forster, K., Friedman, P. G., Le Du, J., Mazure, A., Morrissey, P., Neff, S. G., Schiminovich, D., & Wyder, T. K. 2008, *ApJL*, 683, L131
- Grassberg, E. K., Imshennik, V. S., & Nadyozhin, D. K. 1971, *Ap&SS*, 10, 28
- Grevesse, N. & Sauval, A. J. 1998, *Space Science Reviews*, 85, 161

- Hamuy, M., Pinto, P. A., Maza, J., Suntzeff, N. B., Phillips, M. M., Eastman, R. G., Smith, R. C., Corbally, C. J., Burstein, D., Li, Y., Ivanov, V., Moro-Martin, A., Strolger, L. G., de Souza, R. E., dos Anjos, S., Green, E. M., Pickering, T. E., González, L., Antezana, R., Wischnjewsky, M., Galaz, G., Roth, M., Persson, S. E., & Schommer, R. A. 2001, *ApJ*, 558, 615
- Haubois, X., Perrin, G., Lacour, S., Verhoelst, T., Meimon, S., Mugnier, L., Thiébaud, E., Berger, J. P., Ridgway, S. T., Monnier, J. D., Millan-Gabet, R., & Traub, W. 2009, *A&A*, 508, 923
- Hillier, D. J. & Dessart, L. 2012, *MNRAS*, 424, 252
- Hillier, D. J. & Miller, D. L. 1998, *ApJ*, 496, 407
- Hoeflich, P. 1988, *Proceedings of the Astronomical Society of Australia*, 7, 434
- Jerkstrand, A., Fransson, C., Maguire, K., Smartt, S., Ergon, M., & Spyromilio, J. 2012, *A&A*, 546, A28
- Josselin, E. & Plez, B. 2007, *A&A*, 469, 671
- Kasen, D., Thomas, R. C., Röpke, F., & Woosley, S. E. 2008, *Journal of Physics Conference Series*, 125, 012007
- Kasen, D. & Woosley, S. E. 2009, *ApJ*, 703, 2205
- Kozma, C. & Fransson, C. 1992, *ApJ*, 390, 602
- . 1998a, *ApJ*, 496, 946
- . 1998b, *ApJ*, 497, 431
- Leonard, D. C., Filippenko, A. V., Gates, E. L., Li, W., Eastman, R. G., Barth, A. J., Bus, S. J., Chornock, R., Coil, A. L., Frink, S., Grady, C. A., Harris, A. W., Malkan, M. A., Matheson, T., Quirrenbach, A., & Treffers, R. R. 2002, *PASP*, 114, 35
- Levesque, E. M., Berger, E., Kewley, L. J., & Bagley, M. M. 2010, *AJ*, 139, 694
- Levesque, E. M., Massey, P., Olsen, K. A. G., Plez, B., Josselin, E., Maeder, A., & Meynet, G. 2005, *ApJ*, 628, 973
- Li, C., Hillier, D. J., & Dessart, L. 2012, *MNRAS*, 426, 1671
- Li, H. & McCray, R. 1992, *ApJ*, 387, 309
- . 1993, *ApJ*, 405, 730
- Litvinova, I. I. & Nadezhin, D. K. 1983, *Ap&SS*, 89, 89
- Litvinova, I. Y. & Nadezhin, D. K. 1985, *Soviet Astronomy Letters*, 11, 145
- Livne, E. 1993, *ApJ*, 412, 634
- Lucy, L. B. 1991, *ApJ*, 383, 308
- Maeder, A. & Meynet, G. 1987, *A&A*, 182, 243
- . 2000, *A&A*, 361, 159
- Maguire, K., Jerkstrand, A., Smartt, S. J., Fransson, C., Pastorello, A., Benetti, S., Valenti, S., Bufano, F., & Leloudas, G. 2012, *MNRAS*, 420, 3451
- Meakin, C. A. & Arnett, D. 2007, *ApJ*, 667, 448
- Neilson, H. R., Lester, J. B., & Haubois, X. 2011, in *Astronomical Society of the Pacific Conference Series*, Vol. 451, *Astronomical Society of the Pacific Conference Series*, ed. S. Qain, K. Leung, L. Zhu, & S. Kwok, 117
- Pastorello, A., Sauer, D., Taubenberger, S., Mazzali, P. A., Nomoto, K., Kawabata, K. S., Benetti, S., Elias-Rosa, N., Harutyunyan, A., Navasardyan, H., Zampieri, L., Iijima, T., Botticella, M. T., Di Rico, G., Del Principe, M., Dolci, M., Gagliardi, S., Ragni, M., & Valentini, G. 2006, *MNRAS*, 370, 1752
- Paxton, B., Bildsten, L., Dotter, A., Herwig, F., Lesaffre, P., & Timmes, F. 2011, *ApJS*, 192, 3
- Paxton, B., Cantiello, M., Arras, P., Bildsten, L., Brown, E. F., Dotter, A., Mankovich, C., Montgomery, M. H., Stello, D., Timmes, F. X., & Townsend, R. 2013, *arXiv:1301.0319*
- Popov, D. V. 1993, *ApJ*, 414, 712
- Pumo, M. L. & Zampieri, L. 2011, *ApJ*, 741, 41
- Quataert, E. & Shiode, J. 2012, *MNRAS*, 423, L92
- Quimby, R. M., Wheeler, J. C., Höflich, P., Akerlof, C. W., Brown, P. J., & Rykoff, E. S. 2007, *ApJ*, 666, 1093
- Smartt, S. J. 2009, *ARA&A*, 47, 63
- Smith, N., Hinkle, K. H., & Ryde, N. 2009, *AJ*, 137, 3558
- Smith, N., Li, W., Filippenko, A. V., & Chornock, R. 2011, *MNRAS*, 412, 1522
- Timmes, F. X. 1999, *ApJS*, 124, 241
- Utrobin, V. P. 2007, *A&A*, 461, 233
- Utrobin, V. P. & Chugai, N. N. 2005, *A&A*, 441, 271
- . 2008, *A&A*, 491, 507
- . 2009, *A&A*, 506, 829
- Weaver, T. A., Zimmerman, G. B., & Woosley, S. E. 1978, *ApJ*, 225, 1021
- Wittkowski, M., Hauschildt, P. H., Arroyo-Torres, B., & Marcaide, J. M. 2012, *A&A*, 540, L12
- Woosley, S. E. & Heger, A. 2007, *Phys. Rep.*, 442, 269
- Woosley, S. E., Heger, A., & Weaver, T. A. 2002, *Reviews of Modern Physics*, 74, 1015
- Yoon, S.-C. & Cantiello, M. 2010, *ApJL*, 717, L62
- Young, T. R. 2004, *ApJ*, 617, 1233